إقـــرار

أنا الموقع أدناه مقدم الرسالة التي تحمل العنوان:

Elecromagnatic at Grahpene– Left Handed Waveguide Structures

دراسة الموجات الكهرومغناطيسية في طبقات تحتوي الجرافين ومواد فوق العادة

أقر بأن ما اشتملت عليه هذه الرسالة إنما هي نتاج جهدي الخاص، باستثناء ما تمت الإشارة إليه حيثما ورد، وإن هذه الرسالة ككل، أو أي جزء منها لم يقدم من قبل لنيل درجة أو لقب علمي أو بحثي لدى أية مؤسسة تعليمية أو بحثية أخرى.

DECLARATION

The work provided in this thesis, unless otherwise referenced, is the researcher's own work, and has not been submitted elsewhere for any other degree or qualification

التوقيع: Signature:

التاريخ: Date:

Islamic University of Gaza
Research and Graduate Affairs
Faculty of Science
Department of Physics

ELECTROMAGNETIC WAVES AT GRAPHENE LEFT-HANDED WAVEGUIDE STRUCTURES

BY

Khoulud Khalil I. Abu Shaar

Supervisor

Prof. Dr. Mohammed M. Shabat

Submitted to the Faculty of Science as a Partial Fulfillment of the Master of Science (M. Sc.) in Physics

1436 - 2015

بسم الله الرحمن الرحيم

الجامعة الإسلامية – غزة
The Islamic University - Gaza

مكتب نائب الرئيس للبحث العلمي والدراسات العليا هاتف داخلي 1150

الرقم ج.س.غ/35/..... Ref

التاريخ 2015/04/15/..... Date

نتيجة الحكم على أطروحة ماجستير

بناءً على موافقة شئون البحث العلمي والدراسات العليا بالجامعة الإسلامية بغزة على تشكيل لجنة الحكم على أطروحة الباحثة/ **خلود خليل إبراهيم أبوشعر** لنيل درجة الماجستير في **كلية العلوم** قسم **الفيزياء** وموضوعها:

دراسة الموجات الكهرومغناطيسية في طبقات تحتوي الجرافين ومواد فوق العادة
Electromagnetic at Graphene-Left Handed Waveguide Structures

وبعد المناقشة العلنية التي تمت اليوم الأربعاء 26 جمادي الآخر 1436هـ، الموافق 2015/04/15م الساعة الواحدة ظهراً بمبني اللحيدان، اجتمعت لجنة الحكم على الأطروحة والمكونة من:

أ.د. محمد موسى شبات	مشرفاً ورئيساً	.....
د. حسين عبد الكريم داود	مناقشاً داخلياً	.....
د. مجدي سالم حمادة	مناقشاً خارجيًا	.....

وبعد المداولة أوصت اللجنة بمنح الباحثة درجة الماجستير في كلية العلوم/ قسم الفيزياء.

واللجنة إذ تمنحها هذه الدرجة فإنها توصيها بتقوى الله ولزوم طاعته وأن تسخر علمها في خدمة دينها ووطنها.

والله ولي التوفيق،،،

مساعد نائب الرئيس للبحث العلمي و للدراسات العليا

أ.د. فؤاد علي العاجز

P.O. Box 108, Rimal, Gaza, Palestine fax: +970 (8) 286 0800 فاكس Tel: +970 (8) 286 0700 ص.ب. 108 الرمال، غزة، فلسطين هاتف
public@iugaza.edu.ps www.iugaza.edu.ps

All praise to Allah, today we fold the days tiredness and the errand summing up between the cover of this humble work

To the utmost knowledge lighthouse, to our greatest and most honored prophet Mohamed - May peace and grace from Allah be upon him

To the Spring that never stops giving, who weaves my happiness with strings from her merciful heart... to my dear mother

To whom he strives to bless comfort and welfare and never stints what he owns to push me in the success way,, To the big heart my dear father

To whose love flows in my veins, and my heart always remembers them, to my brothers and sisters

To those who reworded to us their knowledge simply and from their thoughts made a lighthouse guides us through the knowledge and success path, To our honored teachers and professors

To the taste of the most beautiful moments with my friends

I guide this research

Khoulud Kh. Abu Shaar

Acknowledgements

First and foremost I offer my sincerest gratitude to my supervisor, Prof. Dr. Mohammed Shabat, who has supported me throughout my thesis with his patience and knowledge. I attribute the level of my Masters degree to his encouragement and effort and without him this thesis, too, would not have been completed or written.

I would like also to thank Dr. Zeyad Al-Sahhar form Department of physics at Al-Aqsa University for fruitful discussion, important suggestions, and continuous support.

In addition, I would like to thank all the staff members of physics department in the Islamic University; indeed they extended a helping hand wherever I asked them to.

Finally, and perhaps most importantly I would like to thank my family for their unwavering support. Mother, Father without you, I certainly would not be where I am today.

ABSTRACT

Graphene material is inherent from carbon, its two-dimensional hexagonal lattice structure (also called honeycomb), which is the thinnest known at all material so far, equivalent to a thickness of one carbon atom only. Although it is considered one of the strongest (stronger) materials known. Developed by Russian Andrei Geim and Konstantin Novoselov in 2004, and both won Nobel Prize in Physics in 2010.

The properties of graphene have attracted the attention of many disciplines. Also the results of several studies in the field of thermodynamics for graphene led to the growing interest for the study of graphene in the areas of optics and photonics to be used in a variety of applications. On the other hand, macroscopic systems that can be analyzed using Maxwell's equations, the study of waves guided by the existing structures on the graphene allow them to better understanding to the incorporated into electromagnetic devices.

In this study, the dispersion relations for two sheets of parallel graphene in over Gigahertz and Terahertz ranges for two ships of polarization of the electromagnetic field are the magnetic field (TM-Modes), and field electrophoresis (TE -Modes) has been investigated.

The behavior of electromagnetic waves in the presence of a layer of the left-handed material between two sheets of parallel graphene has been studied. The total power flow through the structure has been obtained.

In addition, this article discusses the use of guides waves as sensor by the existence of two layers parallel of graphene with the installation of variables for remote sensing applications.

The sensitivity of the sensing of the variables of electric permittivity and the magnetic permeability of the Left-Handed material has been presented. Moreover, the comparison between the layers that contain the Left-handed materials with layers containing insulating material.

It can be concluded that the presence of a layer of left-handed materials between two layers of graphene gives better results for increased the sensitivity, which may be useful in optoelectronics and electromagnetic applications, such as the design of some of optoelectronic devices based on the scope of a private graphene sensors.

الملخص

الجرافين مادة متأصلة ومشتقة من الكربون، ثنائية الأبعاد بنيتها البلورية سداسية (وتسمى أيضا قرص العسل)، وهي أرفع مادة معروفة على الإطلاق حتى الآن، يعادل سمكها ذرة كربون واحدة فقط، ورغم ذلك تعتبر إحدى أقوى (أمتن) المواد المعروفة. طورها العالميين الروسيين أندريه غيم وكونستانتين نوفوسيلوف عام 2004، وحاز كلاهما على جائزة نوبل في الفيزياء سنة 2010.

لقد جذبت خصائص مادة الجرافين اهتمام العديد من التخصصات. كما أدى نتائج دراسات عديدة في مجال الديناميكا الحرارية للجرافين إلى اهتمام متزايد لدراسة الجرافين في مجالات البصريات والضوئيات لاستخدامها في تطبيقات متنوعة. من جهة أخرى، للأنظمة العينية التي يمكن تحليلها باستخدام معادلات ماكسويل، فإن دراسة موجات تسترشد في الهياكل القائمة على الجرافين تسمح لهم لفهم أفضل لكيفية دمجها في الأجهزة الكهرومغناطيسية.

في هذه الأطروحة تم دراسة علاقة التشتت للوحين متوازين من الجرافين في مدى الجيجاهيرتز والتيراهيرتز لحالتين من حالات استقطاب المجال الكهرومغناطيسي هما المجال المغناطيسي المستعرض (TM-Modes)، والمجال الكهربي المستعرض (TE-Modes) . كما تم دراسة سلوك الموجات الكهرومغناطيسية في وجود طبقة من المواد اليسارية بين لوحين متوازيين من الجرافين.

وفي هذه الأطروحة أيضاً تم استخدام مرشدات الموجات كمجس بوجود طبقتين متوازيتين من الجرافين مع تثبيت المتغيرات لتطبيقات الاستشعار عن بعد، وتم أيضاً استعراض حساسية الاستشعار عن بعد لمتغيري السماحية الكهربائية والنفاذية المغناطيسية للمواد اليسارية. وعلاوة على ذلك، تم المقارنة بين الطبقات التي تحتوي على مواد يسارية مع الطبقات التي تحتوي على مادة عازلة.

أظهرت هذه الأطروحة أن وجود طبقة من المادة اليسارية بين طبقتين من الجرافين أعطت نتائج أفضل لزيادة الحساسية، والتي قد تكون ذات فائدة في التطبيقات الإلكترونية الضوئية والكهرومغناطيسية، مثل تصميم بعض الأجهزة البصرية الالكترونية القائمة على الجرافين خاصة في نطاق المجسات.

LIST OF FIGURE CAPTIONS:

CONTENTS

CHAPTER ONE

GRAPHENE AND METMATERIALS CONCEPTS

This chapter is intended to present introduction about graphene, When discovered, the distinctive characteristics, Optical conductivity of Graphene, and the application of graphene. Its also discussed the Metmaterials and optical sensing: there concepts, brief history, and applications.

1.1 Introduction:

Graphene is a rapidly rising star on the horizon of materials science and condensed matter physics. This strictly two-dimensional material exhibits exceptionally high crystal and electronic quality and despite its short history, has already revealed abundance of new physics and potential applications [1-2].Graphene, a single-atom thick layer of covalently bonded carbon atoms, has recently emerged as an alternative for conducting materials in optical systems. Graphene derives its unusual current transport properties from the Dirac cones in its band structure at the six corners of the first Brillouin zone, which can be directly related to the arrangement of the carbon atoms in a two-dimensional honeycomb structure. Having a linear dispersion relation at energies close to the cone's apex, the charge carriers are relativistic quasi-partials (also called Dirac fermions), resulting in superior low-frequency electronic and mechanical properties for a sheet only a single atom thick.

Owing to its unusual electronic spectrum, graphene has led to the emergence of a new paradigm of “relativistic” condensed matter physics, where quantum relativistic phenomena, some of which are unobservable in high energy physics, can now be mimicked and tested in table-top

experiments. More generally, graphene represents a conceptually new class of materials that are only one atom thick and, on this basis, offers new inroads into low-dimensional physics that has never ceased to surprise and continues to provide a fertile ground for applications[1].

Graphene has also been advertised as a versatile material for opto-electronics and terahertz technology, e.g. in solar cells, light-emitting devices, display technology, and ultrafast Photodetectors.

Recently, we got interested in the use of graphene with Metmaterials. Metamaterials are artificially structured materials in which small, subwavelength electric circuits replace atoms as the basic unit of interaction with electromagnetic radiation. The design of appropriate constituents, such as split-ring resonators (SRR), cut wires, and fishnets, allows for effectively homogeneous media with exotic material response, e.g., magnetism at terahertz and optical frequencies, simultaneous negative permittivity and negative permeability (the so-called left-handed materials) [3], giant chirality [4], and slow-light media. They may enable lenses with subwavelength resolution [5], optical systems going beyond the diffraction limit, and reflectionless photonic devices[6].

1.2 Graphene

Graphene is the name given to a flat monolayer of carbon atoms tightly packed into a two-dimensional (2D) honeycomb lattice, and is a basic building block for graphitic materials of all other dimensionalities (Figure1.1)[7].

The discovery of the 2-D graphene sheet has been a surprise to the scientific community because a 2-D crystal was predicted to be thermodynamically unstable. A 2-D crystal is in general hard to grow because as the lateral size of the crystal grows, the thermal vibration also rapidly grows and diverges on a

macroscopic scale, which forces the 2-D crystallites to morph into a stable 3-D structure[8].

Theoretically, graphene (or "2D graphite") has been studied for sixty years[9-11] and widely used for describing properties of various carbon-based materials. On the other hand, although known as integral part of 3D materials, graphene was presumed not to exist in the free state, being described as an "academic" material and believed to be unstable with respect to the formation of curved structures such as soot, fullerenes and nanotubes. All of a sudden, the vintage model turned into reality, when free-standing graphene was unexpectedly found three years ago and, especially, when the follow-up experiments confirmed that its charge carriers were indeed massless Dirac fermions. So, the graphene "gold rush" has begun [1-2].

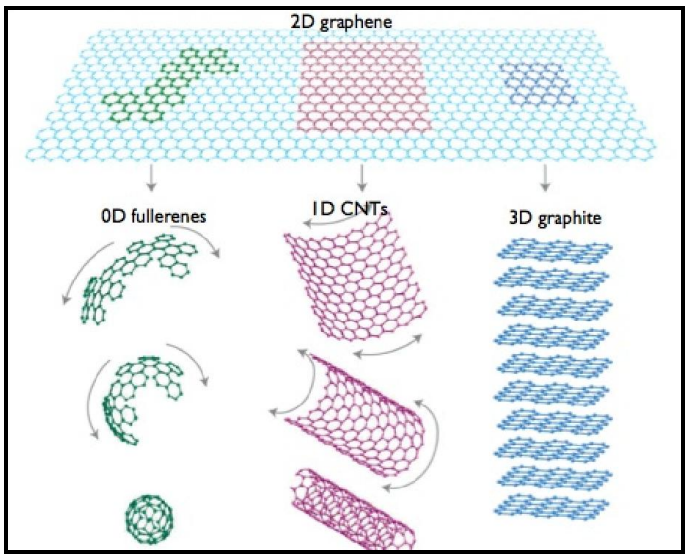

Figure 1.1 Mother of all graphitic forms. Graphene is a 2D building material for carbon materials of all other dimensionalities. It can be wrapped up into 0D Bucky balls, rolled into 1D nanotubes or stacked into 3D graphite[1].

1.2.1 Brief history of graphene

Carbon demonstrates unusually complicated behavior, forming a number of very different structures. As well as diamond and graphite, which have been known since ancient times, recently discovered fullerenes[12-13] and nanotubes are currently a focus of attention for many physicists and chemists. Thus, only 3-dimensional (diamond, graphite), 1- dimensional (nanotubes), and 0- dimensional (fullerenes) allotropes of carbon were known. The two-dimensional form was conspicuously missing, resisting any attempt at experimental observation – until recently[14].

The term graphene first appeared in 1987 to describe single sheets of graphite as one of the constituents of graphite intercalation compounds (GICs) [12-13]. Larger graphene molecules or sheets (so that they can be considered as true isolated 2D crystals) cannot be grown even in principle. In the 1930s, Landau and Peierls (and Mermin, later) showed thermodynamics prevented 2d crystals in free state [15-17].

In 2004: Andre Geim and Kostya Novoselov at Manchester University managed to extract single-atom-thick crystallites (graphene) from bulk graphite[14]: Pulled out graphene layers from graphite and transferred them into thin silicon dioxide on a silicon wafer in a process sometimes called micromechanical cleavage or, simply, the Scotch tape technique. Since 2004, an explosion in the investigation of graphene in term of synthesis, characterization, properties as well as specifically potential application were reported [15].

1.2.2 Properties of Graphene

Graphene is, basically, a single atomic layer of graphite; an abundant mineral which is an allotrope of carbon that is made up of very tightly bonded

carbon atoms organised into a hexagonal lattice. What makes graphene so special is its sp^2 hybridisation and very thin atomic thickness (of 0.345 nm)[18]. These properties are what enable graphene to break so many records in terms of strength, electricity and heat conduction (as well as many others). Graphene has many outstanding properties. Its electrical properties include its high carrier mobility, which is measured in various devices as 8000-10000 cm^2V^{-1} s^{-1} and could reach 200000 cm^2V^{-1} s^{-1} in suspended graphene[19-20]. The one-atom-thick graphene is also found to be impermeable to gases, which could be of interest in bio-molecular and ion transport research[20].

Table 1.1 Summarizes the main properties of graphene.

Parameter	Value and Units
Thermal Conductivity	5000 W/mK
Young's Modulus	1.0 TPa
Mobility (maximum)	200000 cm^2V^{-1} s^{-1}
Saturation Veleocity	4-5 × 10^7 cm/Sec

Table 1.1: Graphene's main properties[19, 21].

1.2.3 Optical Properties

Graphene's ability to absorb a rather large 2.3% of white light is also a unique and interesting property, especially considering that it is only 1 atom thick. This is due to its aforementioned electronic properties; the electrons acting like massless charge carriers with very high mobility. A few years ago, it was proved that the amount of white light absorbed is based on the Fine Structure Constant, rather than being dictated by material specifics. Adding another layer of graphene increases the amount of white light absorbed by approximately the same value (2.3%). Graphene's opacity of $\pi\alpha \approx 2.3\%$

equates to a universal dynamic conductivity value of $G=e^2/4\pi$ (±2-3%) over the visible frequency range[18].

1.2.4 Optical conductivity of Graphene:

The dynamic optical conductivity of graphene σ can be determined from the Kubo formalism[22-23], and an explicit expression for it's conductance:

$$\sigma(\mu_c) = \frac{ie^2(\omega - i\tau^{-1})}{\pi\hbar} \times \left[\frac{1}{(\omega - i\tau^{-1})^2} \int_0^\infty \times \xi \left(\frac{\partial f_d(\xi, \mu_c, T)}{\partial \xi} - \frac{\partial f_d(-\xi, \mu_c, T)}{\partial \xi} \right) - \int_0^\infty \frac{f_d(-\xi, \mu_c, T) - f_d(-\xi, \mu_c, T)}{(\omega - i\tau^{-1})^2 - 4(\xi/\hbar)^2} d\xi \right] \quad (1.1)$$

Where ω is radian frequency, ξ is energy, μ_c is chemical potential, τ is a phenomenological electron relaxation time (τ^{-1} is the scattering rate) that is assumed to be independent of energy, e is the charge of an electron, $\hbar$ is the reduced Planck's constant, and $f_d(\xi, \mu_c, T) = \left(e^{(\xi - \mu_c)/k_B T} + 1\right)^{-1}$ is the Fermi-Dirac distribution, where k_B is Boltzmann's constant and T is temperature.

The first term in Eq.(1.1) is due to intraband contributions, and the second term is due to interband contributions. The intraband term can be evaluated as:

$$\sigma = \sigma_{\text{int}ra} = -i \frac{e^2 k_B T}{\pi\hbar(\omega - i\tau^{-1})} \times \left[\frac{\mu_c}{k_B T} + 2\ln(e^{-\mu_c/K_B T} + 1) \right]. \quad (1.2)$$

With $\sigma = \sigma' + i\sigma''$, it can be seen that $\sigma'_{\text{int}ra} \geq 0$ and $\sigma'_{\text{int}ra} \leq 0$, the imaginary part of conductivity plays an important role in the propagation of surface waves guided by the graphene sheet.

For the Fermi-Dirac statistics [24], $\mu_c / k_B T \gg 1$, the intraband conductivity takes the form[24]:

$$\sigma_{intra} = -i \frac{e^2 \mu_c}{\pi \hbar (\omega - i\tau^{-1})}. \tag{1.3}$$

The interband conductivity can be approximated for $\mu_c / k_B T \gg 1$ as[25]:

$$\sigma_{inter} = -i \frac{e^2}{4\pi\hbar} \times \ln\left[\frac{2|\mu_c| - (\omega - i\tau^{-1})\hbar}{2|\mu_c| + (\omega - i\tau^{-1})\hbar}\right], \tag{1.4}$$

Such that for $\tau^{-1} = 0$ and $2|\mu_c| > \hbar\omega$, $\sigma_{inter} = i\sigma''_{inter}$ with $\sigma''_{inter} > 0$.

For $\tau^{-1} = 0$ and $2|\mu_c| < \hbar\omega$, σ''_{inter} is complex-valued, with[26]:

$$\sigma'_{inter} = \frac{\pi e^2}{2h} = \sigma_{min} = 6.085 \times 10^{-5} \tag{1.5}$$

1.2.5 Application of Graphene:

1.2.5.1 Graphene Energy Stores Application

Energy production and storage are both critical research domains where increasing demands for the improved performance of energy devices and the requirement for greener energy resources constitute immense research interest.

Graphene has incurred intense interest since its freestanding form was isolated in 2004, and with the vast array of unique and highly desirable electrochemical properties it offers, comes the most promising prospects when implementation within areas of energy research is sought[27].

1. Supercapacitors

Supercapacitors attracted considerable attention as energy storage devices; they offer high power density, fast charge-discharge processes and excellent cyclic stability[28]. Generally Supercapacitors were classified into two main types, namely electrical double-layer capacitors and pseudocapacitors. Carbon based materials are widely used as electrode materials in double-layer capacitors owing to their excellent physic-chemical properties[29]. Likewise, graphene based composite materials were had extensive applications in supercapacitors research filed.

Graphene based nancomposites with conduction polymers and metal oxides have been utilized for the applications in pseudocapacitors[30].

2. Batteries

Batteries are extensively used in automobiles (cars and bikes), aircrafts, boats, ships and electronic equipments[31-32]. In this connection, energy demands were considerably increasing every year and hence electrical storage devices having long life, good stability and safety are wanted to fulfill the energy demands[4]. Lithium-ion batteries are one of the promising energy storage devices which can be used in portable electronic applications. Recently, graphene and its composite materials were employed as novel electrode materials for the lithium-ion battery applications. The excellent properties of graphene and ease of fabrication towards preparation of graphene based composites with metal, metal oxides and polymers make them extraordinary materials in the field of batteries[30].

3. Fuel Cell

During the last two decades, carbon nanotubes were evolved as one of the most important nonmaterial towards fuel cell applications[33-34]. Fuel cell are

a kind of energy storage device, which converts chemical energy from a fuel into electrical energy by using oxygen and methanol. After the discovery of graphene, it finds widespread applications in fuel cells, where it can be used as an excellent electrode material ascribed to its excellent physicochemical properties.

4. Solar Cells

Solar Cells (polymer, bulk heterojunction and dye-sensitized) are most important promising devices for the conversion of sun light into electrical energy, offer the advantages of low cost and large scale production. Platinum is widely used as cathode electrode dye-sensitized solar cells (DSSC) applications. Though Platinum has the advantage of having excellent electrocatalytic properties, it is highly expensive. Therefore, researchers have focused on alternative electrode materials example, inexpensive materials to facilitate the similar properties of platinum. Electrode materials based on carbon based materials such as, carbon nanotubes, activated carbon and graphene sheets have high electrocatalytic properties and they could replace the expensive Pt electrode in DSSC applications[30, 35].

1.2.5.2 Graphene Sensors Application

Sensors are widely used in our daily life and its applications becoming increasing in electrochemical, biological and environmental detectives. Sensors studies have been widely used in many fields, such as industry (pollutant), research institute (radiation measurements) and clinical diagnosis[30].

1. Electrochemical Sensors

Electrochemical sensors offer selectivity and sensitivity with very low detection limits ranging from nanomolar to picomolar. A number of

electrochemical techniques including cyclic voltammetry, differential pulse voltammetry and chronoamperometry were employed to study the electrochemical sensors. Graphene based materials have considerable attention for the fabrication of non-enzymatic sensors due to their low cost, high catalytic ability and good stability[5, 30, 37].

2. Biosensors

Biosensors are one of the most important section of sensors, which use biological components to detect the analytes[38]. Electrochemical biosensors developed based on graphene and carbon nanotubes were extensively studied[39-40]. On the other hand, rapid analysis of enzyme based biosensors were widely used biological species in vivo and in vitro. Graphene based biosensors were extensively studied owing to the large specific area, good electrical, thermal and bio-compatibility properties of graphene[3, 30].

3. Pesticide Sensors

Pesticide sensors were broadly used in the field of agriculture production and control of pests and insecticide. Organphosphorous pesticides pollute the environment[41], ground water and affect directly or indirectly through the food process and drinking water. It can cause short and long time health problems leading to death and therefore development of sensitive and selective pesticide sensors are very important[42].

In the past years, different electrodes were demonstrated such as, multi-walled carbon nanotubes, metal oxide composites and polymer nancomposites for the determination of pesticides.

Recently, graphene based composite materials find widespread fame among other carbon materials for the detection of pesticides[30, 43].

1.3 Metmaterials

In the last few years, there has been an increased interest in the scientific community in the study of metamaterials. Metamaterials are a class of composite materials artificially constructed to exhibit exceptional properties not readily found in nature. In particular, there has been high level interset in studying materials which can be characterized by simultaneously negative permittivity and permeability over a certain frequency band[44].

In electromagnetism (EM), electric permittivity (ε), and magnetic permeability (μ) are the two fundamental parameters characterizing the EM property of a medium. Physically, permittivity (permeability) describes how an electric (magnetic) field affects, and is affected by a medium, which is determined by the ability of a material to polarize in response to the electric (magnetic) field. We use the ‘‘material parameter space’’ as shown in Fig. 1.2 to represent all materials, as far as EM properties are concerned[45].

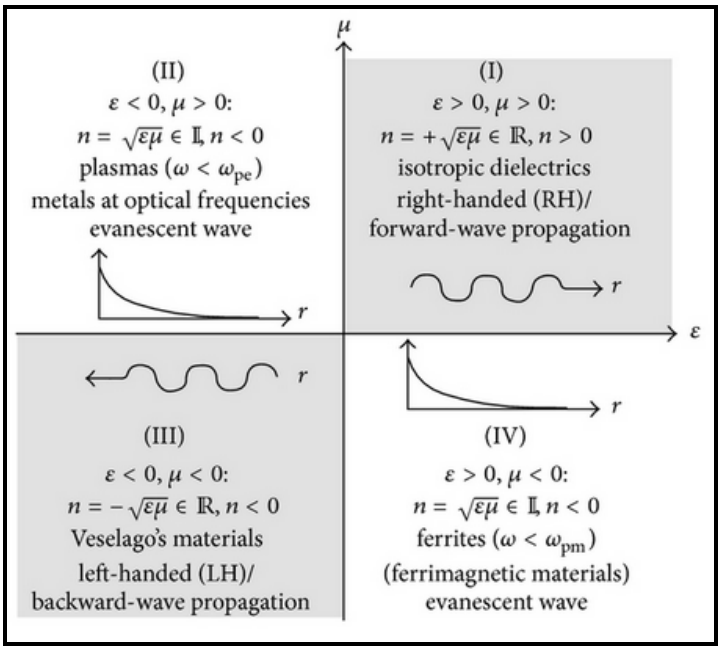

Figure 1.2 Material parametr space characterized by electric permitivity(ε) and magnetic permeablity (μ)[46].

In 1968, V. G. Veselago [47] theoretically investigated the electrodynamics of so-called left-handed, or doubly-negative substances. These materials are defined by simultaneous negative values for the electric permittivity ε and the magnetic permeability μ. He predicted that the wave vector k of a wave propagating through a left-handed substance is antiparallel to its Poynting-vector $\boldsymbol{S}$, as pictured in Fig.1.3 This remarkable property has far-reaching consequences[47].

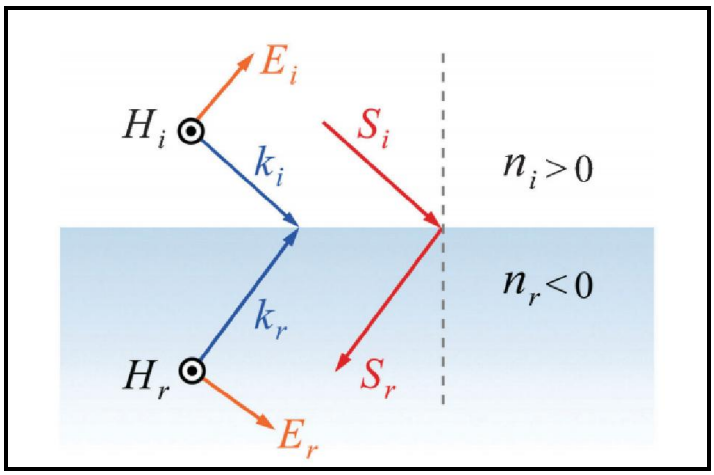

Fig.1.3: Schemmatiac of negative refreaction at the interface between a postitive-index material and a negaive-index material. Note in the negative-index material, the wave vector k Poynting vector S are antiparallel; while in the positive-index material, they are parallel[45].

The prefix "meta" (μετα Greek) means "beyond", and in this sense the name "metamaterials" signifies sytems that are beyond conventional materials. The word "metamaterial" first apeared in literature in 2000 when Smith et al. published their seminal paper on a strucutred material with simultaneously negative permeability and permittivity at microwave frequencies[48].

1.3.1 Negative Refractive index:

Due to its peculiarity in its double negative materilas (DNG) values, where the permittivity ε and a magnetic permeability μ are bouth negative, many other properites of this material are altered altogehter. The most obvious alteration is the refractive index where it takes on a negative value as given by the formula [49-50].

$$n = \pm\sqrt{\varepsilon\mu} \tag{1.6}$$

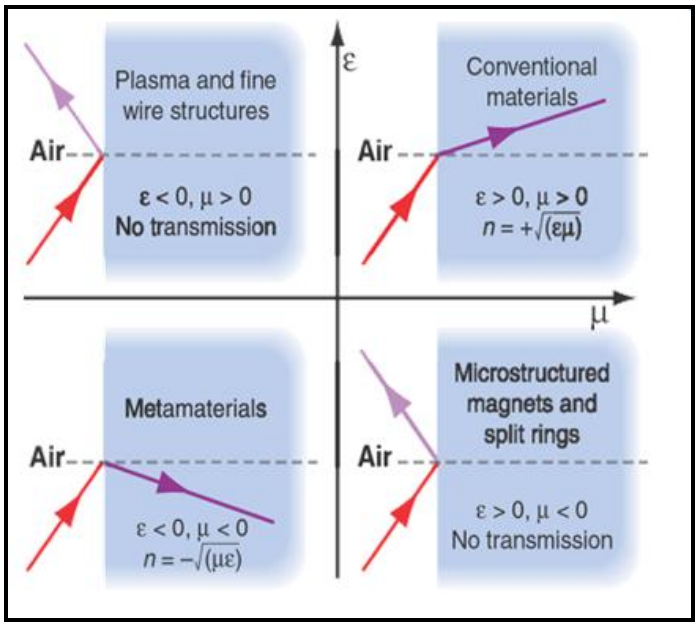

Figure 1.4: Refracted Ray in ε-μ Diagram.

Here, the positive sign is used for the usual case, whereas the negative sign is used when $\varepsilon<0$ and $\mu<0$. At $n=-\sqrt{\varepsilon\mu}$ the LHMs are referred to as negative index materials (NIMs).

The metamaterials with negative refraction index have interesting phenomena that do not appear in natural media can be observed. Among them there are some of unusual properties of waves in LHMs with negative *n* [50, 53]:

- Snell's law ($n_1 \sin\theta_1 = n_2 \sin\theta_2$) still applies, but as n_2 is negative, the rays will be refracted on the same side of the normal on entering the material.
- The Doppler shift is reversed: that is, a light source moving toward an observer appears to reduce its frequency.
- Cherenkov radiation points the other way.

For plane waves propagating in such metamaterials, the electric filed, magnetic filed and Poynting vector (or group velocity) follow a left- hand rule.

1.3.2 A brief Historical Review:

Since Victor Vesalago (1968) [47], a Russian physicist made a theoretical speculation on the existence of substances with simultaneously negative μ and ε, which serves as the origin of all research on LHM.

However, there was not much progress until year 1999 when Prof J. B Pendry [54] proposed his design of Thin-Wire (TW) structure that exhibits the negative value of permittivity and the Split Ring Resonator (SRR) with a negative permeability μ value.

Following this interesting discovery, Dr. Smith (2000) [55] from Duke University combined the two structures and became the first to fabricate the LHM in his lab.

Kong (2002) [56] investigated the electromagnetic wave interaction with stratified media and then specialize to slabs of negative isotropic media. He

investigated field solution of guided waves, the transmission and reflection beams, and linear and dipole antennas in stratified structure of LHMs.

In 2003, Engheta [57] provided the salient electromagnetic features of LHMs, potential future applications, physical remarks, and intuitive justification.

Chew in 2005 [58] studied the energy conservation property and loss condition of a LHM and solve the realistic Sommerfeld problem of a point source over a LHM half space and a LHM slab.

In 2007 Sabah et al. [59] presented the electromagnetic wave propagation through frequency-dispersive and lossy double-negative slab embedded between two different semi-infinite media.

Subsequently, with the paths paved by the pioneers, more and more researchers emerged to study this peculiar material in many fields, for instance .. in filters, absorbers, lens, microwave components, and antenna.

After the experiment demonstration of such materials, the properties and possible applications of various metamaterials with negative index of refraction gained a rapidly increasing interest.

1.3.3 Applications of Metamaterials

There are many applications for found Metamaterials, due to the exciting and unusual properties.

1- Lenses:

The most exciting possible application is the perfect lens. Compared to a conventional convex lens, the LHM lens looks quite exotic in that it does not

have any axis or curvature, nor does it focus parallel rays or magnify small objects. A perfect lens can be used in medical imaging, optical imaging and nondestructive detections [47].

2- Electromagnetic cloaking devices

LHMs also played a pivotal role in the practical realization of an invisibility cloak. The cloak is designed for operation over a narrow band of microwave frequencies and substantially decreases forward and backward scattering from the object[60].

3- Super lenses

A superlens uses metamaterials to achieve resolution beyond the diffraction limit. The diffraction limit is inherent in conventional optical devices or lenses. The first superlens in the microwave regime was realized in 2004[61], which demonstrated resolution three times better than the diffraction limit.

▪ The LHMs can be used in other application areas such as filters, absorber, leak wave antenna, coupler.

1.4 Optical Sensing

Optical Sensors utilize the modification of measured to optical properties such as intensity, phase, and polarization of an input optical signal. Optical sensors have attracted considerable attention, and have excellent advantages such as good compactness and robustness, immunity to electromagnetic interface, high sensitivity, shorter response time, low cost, and high compatibility with optical waveguide sensors [62]. Optical sensors are used for optical communication and made of transparent dielectrics whose function is to guide visible and infrared light over long distance. Sensors based on the design and fabrication of a physical transducer that can transform the chemical

or biological reaction into a measurable signal. Sensing is performed by the evanescent penetration of the field in the cover medium, and is proportional to the fraction of evanescent power flow in the cover. Due to their impotence in bio-sensing application, various optical sensors based on evanescent wave concept have been developed[63].

Optical Sensing is mainly used in monitoring, measuring traces of chemicals and studying all physical and chemical properties that change in accordance with changes in refractive index which depends on film thickness and refractive indices of both film and surroundings.

1.4.1 Sensors process of the Planer Waveguide:

The sensing process of the planar waveguide sensors is performed by the evanescent tail of the modal field in the cover medium[64]. The electromagnetic field guided of the waveguide mode extends as an evanescent field into the substrate and cladding media and senses an effective refractive index of the guided mode[65]. The effective refractive index of a waveguide structure depends on the guided layer thickness, dielectric permittivity and magnetic permeability of the media constituting the waveguide[64]. So, any change in the refractive index of the covering medium leads to a change in the effective refractive index of the guiding mode. The sensing principle of the planar waveguide sensor is to determine the change in the effective refractive index of the covering medium[66].

Many theoretical and experimental studies have been conducted to improve the sensitivity of planar waveguide sensors. Parriaux and Velduis [64] presented and extensive theoretical analysis for the design of evanescent linear waveguide sensors and derived the conditions for the maximum achievable

sensitivity for both TE and TM polarizations. Shabat et al. [67-71] proposed optical waveguide sensors in which one or both of the surrounding media have an intensity dependent refractive index. It is found that utilizing nonlinear media can enhance the sensitivity of slab waveguide sensors. Taya at al. proposed optical waveguide sensors by using Left-handed materials[72]. Another class of optical waveguide sensor has been proposed with the so-called reverse symmetry design[73].

1.4.2 Surface Sensing

The normalized analysis depends on the distribution of the cover medium, if the cover contains a thin layer, known as an adlayer (or in some literature affinity layer), at the surface of the sensor, then the sensing operation is called the surface sensing. Fig. 1.5, here sensitivity is defined as the change of the effective refractive index with respect to change in adlayer width d_A or the refractive index of the adlayer n_A, such as[64] :

$$S_{d_A} = \frac{\partial N}{\partial d_A}, \qquad S_{n_A} = \frac{\partial N}{\partial n_A}. \tag{1.7}$$

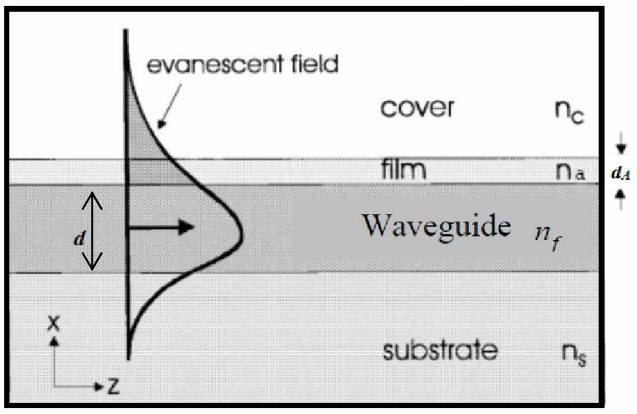

Fig. 1.5. Schematic representation of planar waveguide surface sensor[64].

1.4.3 Homogeneous Sensing

If the cover medium is homogeneously distributed, the process is called homogeneous sensing. Fig. 1.6, the cover sensitivity is defined as the change of the effective refractive index with respect to the change of the cover index[64]:

$$S_{n_c} = \frac{\partial N}{\partial n_c}. \tag{1.8}$$

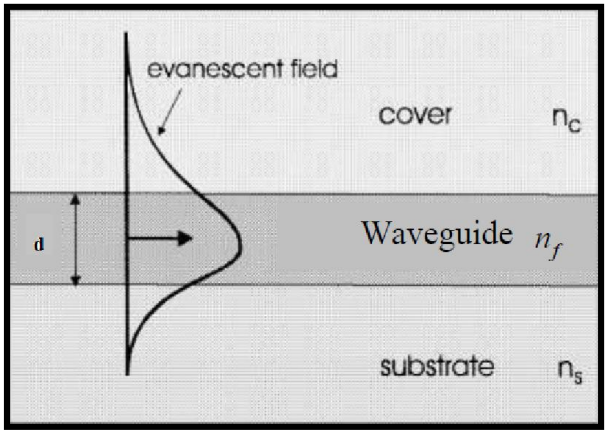

Fig.1.6. Schematic representation of planar waveguide homogeneous sensor[64]

The sensitivity to changes in the cover can be found by [74]:

$$S_{n_c} = \frac{\partial N}{\partial n_c} = \frac{p_c}{P_T}\left[\sqrt{\frac{l-\alpha_c}{1-X}} + 2p\sqrt{\frac{1-X}{1-\alpha_c}} - \sqrt{\frac{l-\alpha_c}{1-X}}\right]. \tag{1.9}$$

where (p_c / P_T)is the fraction of modal power located in the cover layer.

p = 0 for TE and p =1 for TM mode.

And $\alpha_c = 1 - \left(\frac{n_c}{n_f}\right)^2$, $X = 1 - \left(\frac{N}{n_f}\right)^2$. (1.10)

and p number of mode order.

It can observe from equation (1.9):

- If $(\alpha \cong \alpha_s = \alpha_c \ , \ X \ \to \alpha)$, then $S \to \frac{p_c}{P_T} \to 0.5$,
- If $\alpha_C > \alpha_s \ , \ X \ \to \alpha_c$, then $S \to \frac{p_c}{P_T} \to 1$,
- And finally, for $\alpha_s > \alpha_c \ , \ X \ \to \alpha_s$ it turns out that $S \to 0$ since in that case $\frac{p_c}{P_T} \to 0$.

1.4.4 Uses and applications

In recent years several planer optical waveguide sensors have been suggested for biological applications. The detection of pathogenic bacteria have received renewed interest, especially within the fields of food safety, medical diagnostics, and biological warfare. Typically, optical waveguide sensors are used for measuring the refractive index of liquids or various aqueous solutions of biological substances, such as mammalian cells, bacterial cells, and proteins[65, 73].

There are another application for optical waveguide sensors that can be used for detecting and measuring the thickness of layers such as metals, metal compounds, organic, bio-organic, enzymes, antibodies and microbes[75].

They are also used in radiation dosimeters and protective masks or clothing when they can readily identify and five scanning data about any change in exposure or lack in protection.

CHAPTER TWO

FOUNDATIONS OF WAVEGUIDES

This chapter presents the fundamental concepts of electromagnetic theory, and boundary conditions. Wave phenomena are of essential importance for our work. Plane waves are the simplest form of electromagnetic waves and so serve to illustrate a number of basic properties associated with wave propagation. We start this chapter with Maxell's equations, which can be simplified to the geometrical optics regime, and optical systems can be designed with the theory of geometrical optics. Such techniques are sometimes applicable to millimeter wave systems, where they are referred to as quasi-optical.

2.1 Maxwell's equations:

Classical macroscopic electromagnetic phenomena are governed by a set of vector equations known collectively as Maxell's equations [76].

We will start having a look at the Maxwell equations in the SI system of units for matter with $\sigma \neq 0$. The Maxwell's equations read:

$$\nabla \cdot \boldsymbol{D} = \rho, \tag{2.1}$$

$$\nabla \times \boldsymbol{E} = -\frac{\partial \boldsymbol{B}}{\partial t}, \tag{2.2}$$

$$\nabla \cdot \boldsymbol{B} = 0, \tag{2.3}$$

$$\nabla \times \boldsymbol{H} = \boldsymbol{J} + \frac{\partial \boldsymbol{D}}{\partial t}, \tag{2.4}$$

Where $\boldsymbol{D}$, $\boldsymbol{E}$, $\boldsymbol{B}$, $\boldsymbol{H}$, $\boldsymbol{J}$, and ρ the electric displacement, the electric field intensity, the magnetic flux density, the magnetic field intensity, the current

density (current per unit area), and the free charge density (charge per unit volume), respectively.

Consider isotropic, linear and non-dispersive media, the constitutive relations can be written as

$$\boldsymbol{D} = \varepsilon \boldsymbol{E}, \tag{2.5}$$
$$\boldsymbol{B} = \mu \boldsymbol{H}. \tag{2.6}$$

Where ε is the relative dielectric permittivity, and μ is the magnetic permeability, which can be defined as

$$\varepsilon = \varepsilon_0 \varepsilon_r, \tag{2.7}$$
$$\mu = \mu_0 \mu_r. \tag{2.8}$$

ε_0 and μ_0 are the vacuum dielectric and magnetic permeability, ε_r and μ_r are the relative permittivity and permeability of the medium.

Denoting the velocity of light in a vacuum as c_0 , we obtain:

$$\varepsilon_0 = \frac{1}{c_0^2 \mu_0} \approx 8.854188 \times 10^{-12} \quad F/m, \tag{2.9}$$
$$\mu_0 = 4\pi \times 10^{-7} \qquad H/m. \tag{2.10}$$

The current density J (in amperes per square meter) in a conductive material is given by

$$J = \sigma E. \tag{2.11}$$

In an isotopic medium, the wave propagation without free charges and conduction current are most relevant i.e. $\rho = 0$, and $\boldsymbol{J} = 0$.

So, the Eqs. (2.1), (2.2), (2.3) and (2.4) can be written as:

$$\nabla \cdot \boldsymbol{D} = 0, \tag{2.12}$$

$$\nabla \times \boldsymbol{E} = -\frac{\partial \boldsymbol{B}}{\partial t}, \tag{2.13}$$

$$\nabla \cdot \boldsymbol{B} = 0, \tag{2.14}$$

$$\nabla \times \boldsymbol{H} = \frac{\partial \boldsymbol{D}}{\partial t}, \tag{2.15}$$

By using eqs. (2.5) and (2.6) , the above equations also can be written

$$\nabla \cdot \boldsymbol{E} = 0, \tag{2.16}$$

$$\nabla \times \boldsymbol{E} = -\mu \frac{\partial \boldsymbol{H}}{\partial t}, \tag{2.17}$$

$$\nabla \cdot \boldsymbol{H} = 0, \tag{2.18}$$

$$\nabla \times \boldsymbol{H} = \varepsilon \frac{\partial \boldsymbol{E}}{\partial t}, \tag{2.19}$$

2.2 Wave Equations:

Assume that an electromagnetic filed oscillates at a single angular frequency ω (in radians per meter). Vector $\boldsymbol{A}$, which designates an electromagnetic filed, is expressed as[77]

$$\boldsymbol{A} = \mathrm{Re}\left\{\bar{\boldsymbol{A}}(r)\exp(i\omega t)\right\}. \tag{2.20}$$

So, can be write the following phasor expressions (same as the above) for the electric filed $\boldsymbol{E}$, the magnetic filed $\boldsymbol{H}$, the electric flux density $\boldsymbol{D}$, and the magnetic flux Density $\boldsymbol{B}$ are as:

$$\boldsymbol{E}(\boldsymbol{r},t) = \mathrm{Re}\left\{\bar{\boldsymbol{E}}(\boldsymbol{r})\exp(i\omega t)\right\}, \tag{2.21}$$

$$\boldsymbol{H}(\boldsymbol{r},t) = \mathrm{Re}\left\{\bar{\boldsymbol{H}}(\boldsymbol{r})\exp(i\omega t)\right\}, \tag{2.22}$$

$$\boldsymbol{D}(\boldsymbol{r},t) = \mathrm{Re}\left\{\bar{\boldsymbol{D}}(\boldsymbol{r})\exp(i\omega t)\right\}, \tag{2.23}$$

$$\boldsymbol{B}(\boldsymbol{r},t) = \mathrm{Re}\left\{\bar{\boldsymbol{B}}(\boldsymbol{r})\exp(i\omega t)\right\}. \tag{2.24}$$

For simplicity, the $\bar{E}, \bar{H}, \bar{D}$ and $\bar{B}$ in the phasor representation can be denote as **E, H, D** and **B**. Using these expressions, which can be written Eqs. (2.1) to (2.4) as:

$$\nabla.(\varepsilon_r \mathbf{E}) = 0, \tag{2.25}$$

$$\nabla \times \mathbf{E} = -\mathrm{i}\omega \mathbf{B} = -\mathrm{i}\omega\mu_0 \mathbf{H}, \tag{2.26}$$

$$\nabla.\mathbf{H} = 0, \tag{2.27}$$

$$\nabla \times \mathbf{H} = \mathrm{i}\omega \boldsymbol{D} = \mathrm{i}\omega\varepsilon \mathbf{E}, \tag{2.28}$$

Where it is assumed that $\mu_r = 1$ and $\rho = 0.$

Eqs. (2.25) to (2.28) represent Maxwell's equations for time harmonic fields in free charge lossless media.

2.2.1 Wave Equation for Electric Field E:

Applying a vectorial rotation operator $\nabla\times$ to Eq. (2.26), we get

$$\nabla \times (\nabla \times \mathbf{E}) = -\mathrm{i}\omega\mu_0 \nabla \times \mathbf{H}. \tag{2.29}$$

Using the Vectorial formula

$$\nabla \times (\nabla \times \mathbf{A}) = \nabla(\nabla \cdot \mathbf{A}) - \nabla^2 \mathbf{A}, \tag{2.30}$$

Then, the Left-hand side of Eq. (2.29) can be written as:

$$\nabla(\nabla \cdot \mathbf{E}) - \nabla^2 \mathbf{E}. \tag{2.31}$$

The symbol ∇^2 is a Laplacian, given in Cartesian coordinates by:

$$\nabla^2 = \frac{\partial^2}{\partial x^2} + \frac{\partial^2}{\partial y^2} + \frac{\partial^2}{\partial z^2}. \tag{2.32}$$

Since Eq.(2.25) can be rewritten as:

$$\nabla \cdot (\varepsilon_r \mathbf{E}) = \nabla \varepsilon_r \cdot \boldsymbol{E} + \varepsilon_r \nabla \cdot E = 0, \tag{2.33}$$

Then can be rewrite as:

$$\nabla \cdot E = -\frac{\nabla \varepsilon_r}{\varepsilon_r} \cdot \boldsymbol{E}. \tag{2.34}$$

Thus, the left-hand side of Eq. (2. 29) becomes

$$-\nabla\left(\frac{\nabla \varepsilon_r}{\varepsilon_r} \cdot \boldsymbol{E}\right) - \nabla^2 \boldsymbol{E}. \tag{2.35}$$

On the other hand, using Eq. (2.28), we get the right-had side of Eq. (2.29)

$$k_0^2 \varepsilon_r \boldsymbol{E}, \tag{2.36}$$

Where k_0 is the wave number in a vacuum and is expressed as

$$k_0 = \omega\sqrt{\varepsilon_0 \mu_0} = \frac{\omega}{c}. \tag{2.37}$$

Thus, for a medium with the relative permittivity ε_r, the vectorial wave equation for the electric filed E is

$$\nabla^2 \boldsymbol{E} + \nabla\left(\frac{\nabla \varepsilon_r}{\varepsilon_r} \cdot \boldsymbol{E}\right) + k_0^2 \varepsilon_r \boldsymbol{E} = 0. \tag{2.38}$$

And using the wave number k in that medium, given by

$$k = k_0 n = k_0\sqrt{\varepsilon_r} = \omega\sqrt{\varepsilon_0 \varepsilon_r \mu_0} = \omega\sqrt{\varepsilon \mu_0}, \tag{2.39}$$

Eq. (2.38) can be rewritten as:

$$\nabla^2 \boldsymbol{E} + \nabla\left(\frac{\nabla \varepsilon_r}{\varepsilon_r} \cdot \boldsymbol{E}\right) + k^2 \boldsymbol{E} = 0. \tag{2.40}$$

When the relative permittivity ε_r is constant in the medium, this vectorial wave equation can be reduced to the Helmholtz equation as:

$$\nabla^2 \boldsymbol{E} + k^2 \boldsymbol{E} = 0. \tag{2.41}$$

2.2.2 Wave Equation for Magnetic Field M:

Similarly the same steps of Wave Equation for Electric Field E, applying a vectorial rotation operator $\nabla\times$ to Eq. (2.28), we get :

$$\nabla \times (\nabla \times \mathbf{H}) = \mathrm{i}\omega\varepsilon_0 \nabla \times (\varepsilon_r \mathbf{E}). \tag{2.42}$$

Thus,

$$\begin{aligned} \nabla(\nabla \cdot \mathbf{H}) - \nabla^2 \mathbf{H} &= \mathbf{i}\omega\varepsilon_0 (\nabla \varepsilon_r \times \boldsymbol{E} + \varepsilon_r \nabla \times \boldsymbol{E}) \\ &= \mathbf{i}\omega\varepsilon_0 (\nabla \varepsilon_r \times \boldsymbol{E}) + \mathbf{i}\omega\varepsilon_0 \varepsilon_r (-\mathbf{i}\omega\mu_0 \boldsymbol{H}) \\ &= \mathbf{i}\omega\varepsilon_0 (\nabla \varepsilon_r \times \boldsymbol{E}) + k_0^2 \varepsilon_r \boldsymbol{H}. \end{aligned} \tag{2.43}$$

Using eq. (2.28), which can be write as:

$$\mathbf{E} = \frac{1}{\mathrm{i}\omega\varepsilon} \nabla \times \mathbf{H} \qquad \Rightarrow \qquad \mathbf{E} = \frac{1}{\mathrm{i}\omega\varepsilon_0\varepsilon_r} \nabla \times \mathbf{H}. \tag{2.44}$$

Where $\varepsilon = \varepsilon_0 \varepsilon_r$ as mention before.

Now by substitute from Eq. (2.44) to Eq. (2.40), we can obtain the vectorial wave equation for the magnetic filed **H**:

$$\nabla^2 \boldsymbol{H} + \frac{\nabla \varepsilon_r}{\varepsilon_r} \left(\nabla \times \mathbf{H} \right) + k^2 \boldsymbol{H} = 0. \tag{2.45}$$

When the relative permittivity ε_r is constant in the medium, this vectorial wave equation can be reduced to the Helmholtz equation as:

$$\nabla^2 \boldsymbol{H} + k^2 \boldsymbol{H} = 0. \tag{2.46}$$

2.3 Power Consideration (Poynting Vectors):

In this section, the time-dependent electric and magnetic fields are expressed as **E**(**r**,*t*) and **H**(**r**,*t*), and the time-independent electric and magnetic fields are expressed [77-78] as $\bar{\boldsymbol{E}}(\boldsymbol{r},t)$ *and* $\bar{\boldsymbol{H}}(\boldsymbol{r},t)$.

Applying a divergence operator $\nabla \cdot$ *to* $\boldsymbol{E} \times \boldsymbol{H}$, we get:

$$\nabla \cdot \left(\boldsymbol{E} \times \boldsymbol{H} \right) = \boldsymbol{H} \cdot \nabla \times \boldsymbol{E} + \boldsymbol{E} \cdot \nabla \times \boldsymbol{H}. \tag{2.47}$$

Substituting Maxwell's equations (2.2) and (2.4) into Eq. (2.47), we get:

$$\begin{aligned} \nabla \cdot \left(\boldsymbol{E} \times \boldsymbol{H} \right) &= -\mu \boldsymbol{H} \cdot \frac{\partial \boldsymbol{H}}{\partial t} - \varepsilon \boldsymbol{E} \cdot \frac{\partial \boldsymbol{E}}{\partial t} + \sigma \boldsymbol{E}^2 \\ &= -\frac{\partial}{\partial t} \left(\frac{1}{2} \varepsilon \boldsymbol{E}^2 + \frac{1}{2} \mu \boldsymbol{H}^2 \right) - \sigma \boldsymbol{E}^2. \end{aligned} \tag{2.48}$$

When Eq.(2.48) is integrated over a volume V, and using Gauss's Law, we get:

$$\begin{aligned} \int_V \nabla \cdot \left(\boldsymbol{E} \times \boldsymbol{H} \right) dV &= \int_S \left(\boldsymbol{E} \times \boldsymbol{H} \right)_n dS \\ &= -\frac{\partial}{\partial t} \int_V \left(\frac{1}{2} \varepsilon \boldsymbol{E}^2 + \frac{1}{2} \mu \boldsymbol{H}^2 \right) dV - \int_V \sigma \boldsymbol{E}^2 \, dV. \end{aligned} \tag{2.49}$$

Where *n* designates a component normal to the surface *S* of volume *V*.

The first two terms of the last equation correspond to the rate of the reduction of the stored energy in Volume *V* per unit time, while the third term corresponds to the rate of reduction of the energy due to Joule heating in volume *V* per unit time.

Thus, the term $\int_S (\boldsymbol{E} \times \boldsymbol{H})_n \, dS$ is considered to be the rate of energy loss through the surface. Thus,

$$\mathbf{S} = \mathbf{E} \times \mathbf{H}. \tag{2.50}$$

Which this equation is expressed the energy that passes through a unit area per unit time. Eq. (2.50) is called a Poynting vector.

$$\begin{aligned}
\langle \mathbf{S} \rangle &= \langle \mathbf{E} \times \mathbf{H} \rangle \\
&= \left\langle \Re\left\{ \bar{\boldsymbol{E}}(r) e^{(i\omega t)} \right\} \times \Re\left\{ \bar{\boldsymbol{H}}(r) e^{(i\omega t)} \right\} \right\rangle \\
&= \left\langle \frac{\bar{\boldsymbol{E}}(r) e^{(i\omega t)} + \bar{\boldsymbol{E}}^*(r) e^{(-i\omega t)}}{2} \times \frac{\bar{\boldsymbol{H}}(r) e^{(i\omega t)} + \bar{\boldsymbol{H}}^*(r) e^{(-i\omega t)}}{2} \right\rangle \\
&= \frac{1}{4} \left\langle \left(\bar{\boldsymbol{E}} \times \bar{\boldsymbol{H}}^* + \bar{\boldsymbol{E}}^* \times \bar{\boldsymbol{H}} + \bar{\boldsymbol{E}} \times \bar{\boldsymbol{H}} e^{(2i\omega t)} + \bar{\boldsymbol{E}}^* \times \bar{\boldsymbol{H}}^* e^{(-2i\omega t)} \right) \right\rangle \\
&= \frac{1}{2} \Re\left\{ \left\langle \bar{\boldsymbol{E}} \times \bar{\boldsymbol{H}}^* \right\rangle \right\}.
\end{aligned} \tag{2.51}$$

Thus, for an electromagnetic wave oscillating at a single angular frequency, the quantity:

$$\boldsymbol{S} = \frac{1}{2} \bar{\boldsymbol{E}} \times \bar{\boldsymbol{H}}^*. \tag{2.52}$$

S defined as a complex Poynting vector and the energy actually propagating is considered to be the real part of it.

To find the total electromagnetic power, we integrate the Poynting vector as surface integral over the entire area bounding the volume.

Thus, for TE modes , we get:

$$\langle \boldsymbol{S} \rangle = \frac{\beta}{2\omega\mu} \left| \bar{\boldsymbol{E}} \right|^2 \hat{k} . \tag{2.53}$$

Similar manner for TM modes:

$$\langle \boldsymbol{S} \rangle = \frac{\beta}{2\omega\varepsilon} \left| \bar{\boldsymbol{H}} \right|^2 \hat{k} . \tag{2.54}$$

For a multilayer waveguide, the power flowing through the structure can be evaluated using:

For TE mode:

$$P_{total} = \frac{\beta}{2\omega} \int_{-\infty}^{\infty} \frac{\left| E_y(x) \right|^2}{\mu(x)} dx ; \tag{2.55}$$

and for TM mode:

$$P_{total} = \frac{\beta}{2\omega} \int_{-\infty}^{\infty} \frac{\left| H_y(x) \right|^2}{\varepsilon(x)} dx ; \tag{2.56}$$

2.4 Boundary Conditions for Electromagnetic Fields:

The boundary conditions required for the electromagnetic fields are summarized as follows[78]:

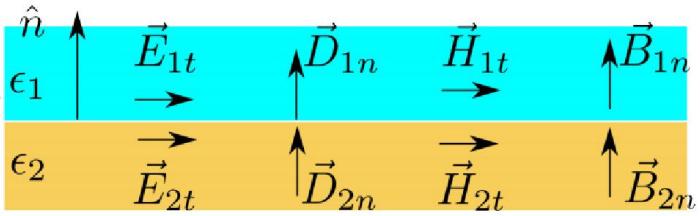

Figure 2.1: Tangential and perpendicular fields at an interface.[79].

(a) Tangential components of the electric fields are continues such that:

$$\hat{n}\times\boldsymbol{E}_{1t}-\hat{n}\times\boldsymbol{E}_{2t}=0,$$
$$\hat{n}\times\boldsymbol{E}_{1t}=\hat{n}\times\boldsymbol{E}_{2t}. \qquad (2.57)$$

(b) When no current flows on the surface, tangential components of the magnetic fields are continues such that

$$\hat{n}\times\boldsymbol{H}_{1t}-\hat{n}\times\boldsymbol{H}_{2t}=0,$$
$$\hat{n}\times\boldsymbol{H}_{1t}=\hat{n}\times\boldsymbol{H}_{2t}. \qquad (2.58)$$

When a current flows on the surface, the magnetic fields are discontinuous and are related to the current density $\boldsymbol{J}_s$ as follows:

$$\hat{n}\times\left(\boldsymbol{H}_{1t}-\boldsymbol{H}_{2t}\right)=\boldsymbol{J}_s. \qquad (2.59)$$

Where the magnetic field and the current are perpendicular to each other.

(c) When there is no charge on the surface, the normal components of the electric flux densities are continuous such that

$$\hat{n}\cdot\boldsymbol{D}_1-\hat{n}\cdot\boldsymbol{D}_2=0,$$
$$D_{1n}=D_{2n}. \tag{2.60}$$

When there are charges on the surface, the electric flux densities are discontinuous and are related to the charge density ρ_S are follow:

$$\hat{n}\times\left(\boldsymbol{D}_1-\boldsymbol{D}_2\right)=\rho_s,$$
$$D_{1n}-D_{2n}=\rho_s. \tag{2.61}$$

(d) Normal components of the magnetic flux densities are continuous such that

$$\hat{n}\cdot\boldsymbol{B}_1-\hat{n}\cdot\boldsymbol{B}_2=0,$$
$$B_{1n}=B_{2n}. \tag{2.62}$$

Note:

1- $\hat{n}$ the unit vector normal to the plane surface and indices 1(2) refer to the first (second) medium.
2- The subscripts n and t in these equations are respectively unit normal and tangential components at the boundary.

2.5 Maxwell's Equations for a plane wave:

By using a Maxwell's equations, we can specify the features of a plane wave propagating in a homogenous nonconductive medium[78].

Consider an electromagnetic wave provided to the optical slab waveguide and propagates in the z-direction, (shown in Fig. 2.2) .

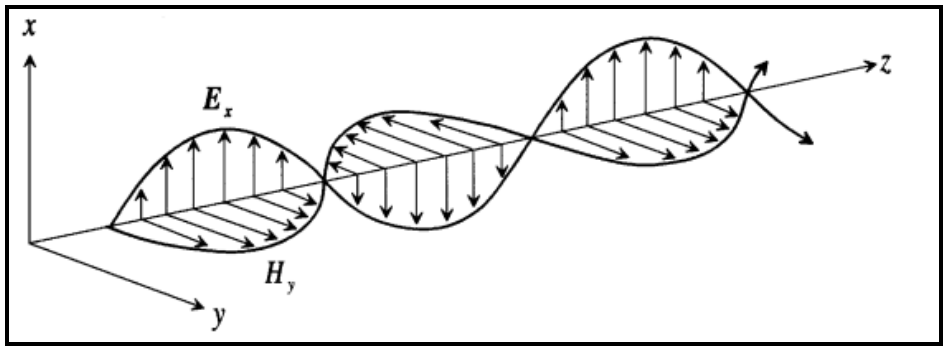

Figure 2.2: Propagation of an electromagnetic field[78].

The electric and magnetic fields are supposed to have the sinusoidal form:

$$\boldsymbol{E} = E_0(x, y)e^{i(\omega t - \beta z)}, \tag{2.63}$$

$$\boldsymbol{H} = H_0(x, y)e^{i(\omega t - \beta z)}, \tag{2.64}$$

Where ω is the frequency of the field and β represents the longitudinal component of the wave vector, and E_0 and H_0 define the amplitude and the direction of the vectors $\boldsymbol{E}$ and $\boldsymbol{H}$, respectively, .

So, by substitute form eq. (2.63) and eq. (2.64) into eq. (2.26) and eq. (2.28) we get :

$$\frac{\partial E_z}{\partial y} - \frac{\partial E_y}{\partial z} = -i\,\omega\mu_0 H_x, \tag{2.65}$$

$$\frac{\partial E_x}{\partial z} - \frac{\partial E_z}{\partial x} = -i\,\omega\mu_0 H_y, \tag{2.66}$$

$$\frac{\partial E_y}{\partial x} - \frac{\partial E_x}{\partial y} = -i\,\omega\mu_0 H_z, \tag{2.67}$$

$$\frac{\partial H_z}{\partial y} - \frac{\partial H_y}{\partial z} = i\,\omega\varepsilon_0\varepsilon_r E_x\,, \tag{2.68}$$

$$\frac{\partial H_x}{\partial z} - \frac{\partial H_z}{\partial x} = i\,\omega\varepsilon_0\varepsilon_r E_y\,, \tag{2.69}$$

$$\frac{\partial H_y}{\partial x} - \frac{\partial H_x}{\partial y} = i\,\omega\varepsilon_0\varepsilon_r E_z\,, \tag{2.70}$$

Since the electric and magnetic fields of the plane wave don't depend on the x and y-coordinates but on the z-coordinate, that means the derivatives with respect to the coordinates for directions other than the propagation direction are zero. That is, $\partial/\partial x = 0$ and $\partial/\partial y = 0$.

The Eqs. (2. 65) – (2.70) becomes

$$\frac{\partial E_y}{\partial z} = i\,\omega\mu_0 H_x\,, \tag{2.71}$$

$$\frac{\partial E_x}{\partial z} = -i\,\omega\mu_0 H_y\,, \tag{2.72}$$

$$\frac{\partial H_y}{\partial z} = -i\,\omega\varepsilon_0\varepsilon_r E_x\,, \tag{2.73}$$

$$\frac{\partial H_x}{\partial z} = i\,\omega\varepsilon_0\varepsilon_r E_y\,, \tag{2.74}$$

Equations (2.71) – (2.74) are categorized into two sets:

Set 1:

$$\frac{\partial E_x}{\partial z} = -i\,\omega\mu_0 H_y\,, \tag{2.75a}$$

and

$$\frac{\partial H_y}{\partial z} = -i\,\omega\varepsilon_0\varepsilon_r E_y\,, \tag{2.75b}$$

Set 2:

$$\frac{\partial E_y}{\partial z} = i\,\omega\mu_0 H_x\,, \tag{2.76a}$$

and

$$\frac{\partial H_x}{\partial z} = i\,\omega\varepsilon_0\varepsilon_r E_y\,, \tag{2.76b}$$

The equations of set 1 can be reduced to:

$$\left(\frac{\partial^2}{\partial z^2} + k^2\right)E_x = 0, \quad and \quad \left(\frac{\partial^2}{\partial z^2} + k^2\right)H_y = 0. \tag{2.77}$$

and the equations of set 2 can be reduced to:

$$\left(\frac{\partial^2}{\partial z^2} + k^2\right)E_y = 0, \quad and \quad \left(\frac{\partial^2}{\partial z^2} + k^2\right)H_x = 0. \tag{2.78}$$

Where $k^2 = \omega^2\varepsilon_0\mu_0\varepsilon_r = k_0^2\varepsilon_r$.

At this section we discuss a plane wave propagating in the z-direction.

The features of the plane wave are summarized as follows [78[:

1- The electric and magnetic fields are uniform in directions perpendicular to the propagation direction, that is , $\partial/\partial x = 0$ and $\partial/\partial y = 0$;
2- The fields have no component in the propagation direction, that is, $H_z = E_z = 0$;
3- The electric field and the magnetic field components are perpendicular to each other;
4- The propagation direction is the direction in which a screw being turned to the right, as if the eclectic field component is being turned toward the magnetic field component, advances.

2.6 Optical Waveguide Modes:

The optical waveguide is the fundamental element that interconnects the various devices of optical integrated circuits, just as a metallic strip does in an electrical integrated circuit. However, unlike electrical current that flows through a metal strip according to Ohm's law, optical waves travel in the waveguide in distinct optical modes. A mode, in this sense, is a spatial distribution of optical energy in one or more dimensions that remains constant in time[80-81].

2.6.1 Modes in Waveguide:

The propagating modes along the waveguide may be classified according to which field components are present or not present in the wave. The field components in the direction of wave propagation are defined as longitudinal components while those perpendicular to the direction of propagation are defined as transverse components.

Assuming the waveguide is oriented with its axis along z-axis (direction of wave propagation), the modes may be classified as[82]:

i- **Transverse Electromagnetic (TEM) modes**: The electric and magnetic fields are transverse to the direction of wave propagation with no longitudinal components [$E_z = H_z = 0$].

- TEM modes cannot exist on single conductor guiding structures. Plane waves can also be classified as TEM modes (as we see before).
- **Quasi-TEM Modes** – modes which approximate true TEM modes when the frequency is sufficiently small.

$$\lim_{f \to 0} E_z = \lim_{f \to 0} H_z = 0$$

ii- **Transverse Electric (TE) modes:** The electric field is transverse to the direction of propagation (no longitudinal electric field component) while the magnetic field has both transverse and longitudinal components [$E_z = 0, H_z \neq 0$].

iii- **Transverse Magnetic (TM) modes:** The magnetic field is transverse to the direction of propagation (no longitudinal magnetic field component) while the electric field has both transverse and longitudinal components [$H_z = 0, E_z \neq 0$].

iv- **Hybrid Modes (EH or HE modes):** Both the electric and magnetic fields have longitudinal components [$E_z \neq H_z \neq 0$]. The longitudinal electric filed is dominant in the EH mode while the longitudinal magnetic field is dominant in the HE mode.

2.7 Parallel Plate Waveguide Structure (PPWG):

Waveguides have many different forms that depend on the purpose of the guide, and on the frequency of the waves to be transmitted. The parallel plate waveguide is the simplest type of guide that can support TM and TE modes. This type of the waveguide it can also support a TEM mode since it is formed from two flat conducting plates, or strips, as shown in Figure 2.4. Although it is an idealization, understating the parallel plate guide can be useful because its operation is similar to that of many other waveguides. The parallel plate guide can also be useful for modeling the propagation of higher order modes in stripline[83].

The following assumptions are made in the determination of the various modes on the parallel plate waveguide:

1- The waveguide is infinite in length (no reflection).

2- The waveguide conductors are Perfect electric conductor (PEC's) and the dielectric is lossless.
3- The plate width is much larger than the plate separation ($w >> d$) so that the variation of the fields with respect to z may be neglected.

A material with permittivity ε and permeability μ is assumed to fill the region between the two plates[83].

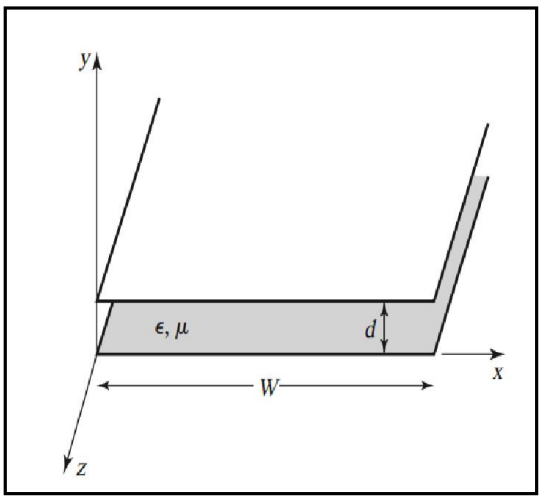

Figure 2.3 : Geometry of a parallel plate waveguide[84].

2.7.1 General waveguides solutions for modes in PPWG:

Now, we discuss an optical waveguide whose structure is a linear, isotropic and homogeneous region, with an $e^{-i\beta z}$ z dependence, the six Maxwell's equations (2.65) – (2.70) can be written as[84]:

$$\frac{\partial E_z}{\partial y} + i\beta E_y = -i\omega\mu H_x, \tag{2.79}$$

$$-i\beta E_x - \frac{\partial E_z}{\partial x} = -i\omega\mu H_y, \tag{2.80}$$

$$\frac{\partial E_y}{\partial x} - \frac{\partial E_x}{\partial y} = -i\omega\mu H_z, \tag{2.81}$$

$$\frac{\partial H_z}{\partial y} + i\beta H_y = i\omega\varepsilon E_x, \tag{2.82}$$

$$i\beta H_x + \frac{\partial H_z}{\partial x} = -i\omega\varepsilon E_y, \tag{2.83}$$

$$\frac{\partial H_y}{\partial x} - \frac{\partial H_x}{\partial y} = i\omega\varepsilon E_z, \tag{2.84}$$

Where β is the propagation constant and is the z-directed component of the wave number k. The ratio of the propagation constant in the medium, β, to the wave number in a vacuum, k_0, is called the effective index:

$$N_{eff} = \frac{\beta}{k_0}, \tag{2.85}$$

We can summarize the Helmholtz equation for the electric field $\boldsymbol{E}$ in eq (2.41) as:

$$\nabla^2 \boldsymbol{E} + (k_j{}^2 - \beta^2)\boldsymbol{E} = 0, \tag{2.86}$$

or

$$\nabla^2 \boldsymbol{E} + \gamma_j^2 \boldsymbol{E} = 0, \tag{2.87}$$

Similarity the Helmholtz equation for the Magnetic field $\boldsymbol{H}$ in eq. (2.45) is as:

$$\nabla^2 \boldsymbol{H} + (k_j{}^2 - \beta^2)\boldsymbol{H} = 0, \tag{2.88}$$

or

$$\nabla^2 \boldsymbol{H} + \gamma_j^2 \boldsymbol{H} = 0, \tag{2.89}$$

Where

$$\gamma_j^2 = k_j^2 - \beta^2. \tag{2.90}$$

γ_j^2: is defined as the cutoff wave number, where $k_j = \sqrt{\varepsilon_j \mu_j}\, k_0$, j =1, 2,3 is the wavenumber in region j, and $k_0 = \omega\sqrt{\mu_0 \varepsilon_0} = \omega / c$ is the free-space wavenumber, and $\varepsilon = \varepsilon_0 \varepsilon_j$, $\mu = \mu_0 \mu_j$, ε_j and μ_j are the relative permittivity and permeability of the region j.

2.7.2 Parallel Plate Waveguide Structure (PPWG) for Transversal Electric mode (TE Mode):

In the TE mode, the electric field is not in the longitudinal direction $(E_z = 0)$ but in the transverse direction $(E_y \neq 0)$. Only three components exist for TE mode E_y, H_x, and H_z. The two magnetic field components H_x and H_z can be expressed in terms of the electric field component E_y by:

$$H_x(x) = -\frac{\beta}{\omega\mu_0} E_y(x), \tag{2.91}$$

$$H_z(x) = -\frac{i}{\omega\mu_0}\frac{d}{dx} E_y(x). \tag{2.92}$$

Substituting from Eqs. (2.91) and (2.929) into Eq. (2.83) gives the wave equation, Helmholtz equation

$$\frac{d^2}{dx^2} E_y(x) + (k_j{}^2 - \beta^2) E_y(x) = 0. \tag{2.93}$$

The *TE* wave impedance can be found as:

$$Z_{TE} = \frac{E_x}{H_y} = -\frac{E_y}{H_x} = \frac{\omega\mu}{\beta} = \sqrt{\frac{\mu}{\varepsilon}} = \eta. \tag{2.94}$$

TE waves can be supported inside closed conductors as well as between two or more conductors.

2.7.3 Parallel Plate Waveguide Structure (PPWG) for Transversal Magnetic mode(TM Mode)

In the TM mode, the magnetic field component is not in the longitudinal direction $(H_z = 0)$ but in the transverse direction $(H_y \neq 0)$. Only three components exist for TM mode H_y, E_x, and E_z. The two electric field components E_x and E_z can be expressed as[86]:

$$E_y(x) = \frac{\beta}{\omega\mu_0} H_y(x), \tag{2.95}$$

$$E_z(x) = -\frac{i}{\omega\varepsilon_0\varepsilon_r}\frac{d}{dx} H_y(x). \tag{2.96}$$

Substituting from Eqs.(2.95) and (2.96) into Eq. (2.80) gives the wave equation, Helmholtz equation:

$$\frac{d^2}{dx^2} H_y(x) + (k_j{}^2 - \beta^2) H_y(x) = 0. \tag{2.97}$$

The fields and propagation constant of the TM mode can be gained by solving for $H_y(x)$ in above equation.

The *TM* wave impedance can be found as:

$$Z_{TM} = \frac{E_x}{H_y} = -\frac{E_y}{H_x} = \frac{\beta}{\omega\mu} = \sqrt{\frac{\mu}{\varepsilon}} = \eta. \tag{2.98}$$

As for *TE* waves, *TM* waves can be supported inside closed conductors as well as between two or more conductors

CHAPTER THREE

Electromagnetic Waves At Graphene Parallel-Plate Waveguide (TM-Mode)

This section is based on the paper "Quasi-transverse electromagnetic modes supported by a graphene parallel-plate waveguides" by Pro. George W. Hanson [87] .

Hanson has developed a modal of parallel-plate waveguide containing graphene. He has represented the graphene as an infinitesimally thin layers. The local two-sided surface characterized by a surface conductivity obtained from the Kubo formula. He used Maxell's equations to solved the model fields guided by graphene layers. He shown that despite the extreme thinness of its walls, a graphene parallel-plate waveguide can guide quasi-transverse electromagnetic modes.

He depicts two laterally infinite graphene sheets spaced a distance d apart and immersed in a layered medium, where all material parameters may have complex values.

Hanson concluded that the graphene is given by the conductivity σ , which can be written as[87]:

$$\sigma = -\frac{je^2(\omega - j\tau^{-1})}{\pi\hbar} \times \left[\frac{\mu_C}{K_B T} + 2\ln\left(e^{-\mu_c/k_B T} + 1\right) \right] \tag{3.1}$$

Where ω is radian frequency, μ_c is chemical potential, τ is a phenomenological electron relaxation time (τ^{-1} is the scattering rate) that is assumed to be independent of energy, e is the charge of an electron, $\hbar$ is the reduced Planck's, k_B is Boltzmann's constant and T is temperature.

3.1 Structure Analysis

We consider a structure consisting infinite graphene sheets spaced a distance *d,* apart and immersed a layered medium, occupying the planes $x = -d/2$ and $x = d/2$ and infinite in *y* and *z* directions. We assume that the electromagnetic wave propagates in the z-direction. So the electric and magnetic field of the propagating waveguide mode will be:

$$\boldsymbol{E}(\mathbf{r},\mathrm{t}) = \boldsymbol{E}_y(x)e^{i(\omega t-\beta z)}, \tag{3.2a}$$

$$\boldsymbol{H}(\mathbf{r},\mathrm{t}) = \boldsymbol{H}_y(x)e^{i(\omega t-\beta z)}, \tag{3.2b}$$

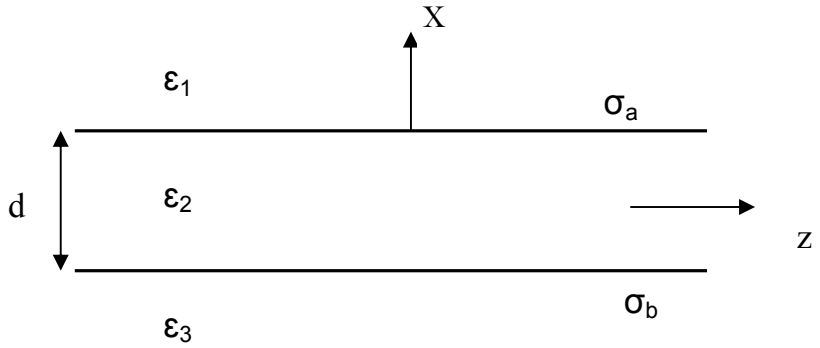

Figure 3.1: Graphene PPWG (Side view) formed by two graphene sheets, each characterized by surface conductance $\sigma_{a,b}$.

In this geometry, two types of waveguide modes can propagate: The TM (p-polarized) modes, and the TE (s-polarized) modes. In the following section the TM mode and is analyzed and discussed.

3.2 The Dispersion Relation:

We consider the TM wave with the magnetic filed perpendicular to the plane of incidence (*xz*), possesses the electromagnetic field components **E** = $\{E_x, 0, E_z\}$, ***H***= $\{0, H_y, 0\}$.

Maxwell's equations require that in the $H_y(x)$ introduced in eqs. (3.1) satisfies:

$$\frac{d^2}{dx^2}H_y(x) + (k_j{}^2 - \beta^2)H_y(x) = 0. \tag{3.3}$$

Where $k_j = k_j = \sqrt{\varepsilon_j}\,k_o$, $j = 1,2,3$ is the wavenumber in region, j, ε_j is the relative permittivity of region j, and $k_o = \omega\sqrt{\mu_o\varepsilon_o} = \omega/c$ is the free-space wavenumber (c is the speed of light in vacuum).

The boundary conditions to be enforced at material interfaces are:

$$\hat{\mathbf{x}} \times (\mathbf{H}_+ - \mathbf{H}_-) = \mathbf{J}^s = \sigma\mathbf{E}, \tag{3.4}$$

$$\hat{\mathbf{x}} \times (\mathbf{E}_+ - \mathbf{E}_-) = 0, \tag{3.5}$$

$$\lim_{x \to \pm\infty} \mathbf{E}, \mathbf{H} = 0, \tag{3.6}$$

Where $\mathbf{J}^s$(A/m) is an electric surface current on the boundary, $\mathbf{E}_+$ and $\mathbf{H}_+$ are the fields on the upper side of the interface, $\mathbf{E}_-$ and $\mathbf{H}_-$ are the corresponding fields on the lower side of the interface, and σ is the interface conductivity (units of SI), $\hat{\mathbf{x}}$ is the normal unit vector to the interface surfaces.

The waveguiding axis is chosen as the z-axis, and from source- free Maxell's equations for the TM^z fields in each region are:

$$\frac{\partial H_y}{\partial z} = -i\,\omega\varepsilon_j\varepsilon_0 E_x\,, \tag{3.7a}$$

$$\frac{\partial H_y}{\partial x} = \quad i\,\omega\varepsilon_j\varepsilon_0 E_z\,, \tag{3.7b}$$

$$\frac{\partial E_x}{\partial z} - \frac{\partial E_z}{\partial x} = -i\,\omega\mu_0 H_y\,, \tag{3.7c}$$

Modal fields are:

$$H_y(x) = \begin{cases} A\,e^{-i\gamma_1 x} & x > d/2 \\ B\,\sin\gamma_2 x + C\,\cos\gamma_2 x & -d/2 \le x \le d/2 \\ De^{i\gamma_3 x} & x < -d/2 \end{cases} \tag{3.8}$$

$$E_z(x) = \begin{cases} -\dfrac{A\gamma_1}{\omega\varepsilon_0\varepsilon_1} e^{-i\gamma_1 x} & x > d/2 \\ -i\,\dfrac{\gamma_2}{\omega\varepsilon_0\varepsilon_2}\left[B\,\cos(\gamma_2 x) - C\,\sin(\gamma_2 x)\right] & -d/2 \le x \le d/2 \\ \dfrac{D\gamma_3}{\omega\varepsilon_0\varepsilon_3} e^{i\gamma_3 x} & x < -d/2 \end{cases} \tag{3.9}$$

Where A, B, C and D are constants with respect to position.

By applied Boundary Conditions (3.5 -3.6):

(1) At x = d/2,

$$H_y^{(1)} - H_y^{(2)} = \sigma_a E_z^{(1)},$$

$$A\,e^{-i\gamma_1 d/2} - \left[B\,\sin(\gamma_2 d/2) + C\,\cos(\gamma_2 d/2)\right] = \sigma_a\left(-\frac{A\gamma_1}{\omega\varepsilon_0\varepsilon_1}\right)e^{-i\gamma_1 d/2},$$

$$B\,\sin(\gamma_2 d/2) + C\,\cos(\gamma_2 d/2) = A\left(1 + \frac{\gamma_1\sigma_a}{\omega\varepsilon_0\varepsilon_1}\right)e^{-i\gamma_1 d/2}, \tag{3.10}$$

$$E_z^{(1)} - E_z^{(2)} = 0,$$

$$\left(-\frac{\gamma_1}{\omega\varepsilon_0\varepsilon_1}\right) A e^{-i\gamma_1 d/2} = \left(-i\,\frac{\gamma_2}{\omega\varepsilon_0\varepsilon_2}\right)\left[B\cos(\gamma_2 d/2) - C\sin(\gamma_2 d/2)\right],$$

$$B\cos(\gamma_2 d/2) - C\sin(\gamma_2 d/2) = -i\left(\frac{\gamma_1\varepsilon_2}{\gamma_2\varepsilon_1}\right) A e^{-i\gamma_1 d/2}, \qquad (3.11)$$

From eq.(3.10) and eq.(3.11) we have get:

$$B = C\,\frac{\sin(\gamma_2 d/2) - ic_a\cos(\gamma_2 d/2)}{\cos(\gamma_2 d/2) + ic_a\sin(\gamma_2 d/2)}, \qquad (3.12)$$

Where

$$c_a = \left(\frac{\varepsilon_2\gamma_1}{\varepsilon_1\gamma_2}\right)\left(1 + \frac{\sigma_a\gamma_1}{\omega\varepsilon_1\varepsilon_0}\right)^{-1}, \qquad (3.13)$$

(2) At x = -d/2,

$$H_y^{(2)} - H_y^{(3)} = \sigma_b E_z^{(3)},$$

$$\left[-B\sin(\gamma_2 d/2) + C\cos(\gamma_2 d/2)\right] - De^{-i\gamma_3 d/2} = \sigma_b\left(\frac{D\gamma_3}{\omega\varepsilon_0\varepsilon_3}\right)e^{-i\gamma_3 d/2},$$

$$-B\sin(\gamma_2 d/2) + C\cos(\gamma_2 d/2) = D\left(1 + \frac{\gamma_3\sigma_3}{\omega\varepsilon_0\varepsilon_3}\right)e^{-i\gamma_3 d/2}, \qquad (3.14)$$

$$E_z^{(2)} - E_z^{(3)} = 0,$$

$$\left(-i\,\frac{\gamma_2}{\omega\varepsilon_0\varepsilon_2}\right)\left[B\cos(\gamma_2 d/2) + C\sin(\gamma_2 d/2)\right] = \left(\frac{\gamma_3}{\omega\varepsilon_0\varepsilon_3}\right)De^{-i\gamma_3 d/2},$$

$$B\cos(\gamma_2 d/2) + C\sin(\gamma_2 d/2) = i\left(\frac{\gamma_3\varepsilon_2}{\gamma_2\varepsilon_3}\right) A e^{-i\gamma_3 d/2}, \qquad (3.15)$$

From eq.(3.14) and eq.(3.15) we have get:

$$B = C\frac{-\sin(\gamma_2 d/2) + ic_b\cos(\gamma_2 d/2)}{\cos(\gamma_2 d/2) + ic_b\sin(\gamma_2 d/2)}, \tag{3.16}$$

Where

$$c_b = \left(\frac{\varepsilon_2\gamma_3}{\varepsilon_3\gamma_2}\right)\left(1+\frac{\sigma_b\gamma_3}{\omega\varepsilon_3\varepsilon_0}\right)^{-1}, \tag{3.17}$$

By solving eq. (3.12) with eq.(3.16) and using Applications of Trigonometric, we have the dispersion equation for the guided modes:

$$\left(c_a + c_b\right)\cos\gamma_2 d + \left(c_a c_b + 1\right) i\sin\gamma_2 d = 0, \tag{3.18}$$

where $\gamma_j^2 = k_j^2 - \beta^2$.

Eq, (3.18) can be written as:

$$\tan\gamma_2 d = i\frac{c_a + c_b}{c_a c_b + 1}. \tag{3.19}$$

3.3 Approximation Solution

Hanson assumed that the graphene PPWG is a perturbation of a perfectly conducting PPWG, and approximation solution had been found as[87]:

$$\tan\gamma_2 d \approx \gamma_2 d, \frac{\sigma_a\gamma_1}{\omega\varepsilon_1\varepsilon_0}, \frac{\sigma_b\gamma_3}{\omega\varepsilon_3\varepsilon_0} \gg 1, \tag{3.20}$$

Appling the mentioned approximation in the dispersion relation, we obtain :

$$\beta / k_0 = \sqrt{\varepsilon_2 \left\{ 1 + \frac{1}{\eta_0^2 \sigma_a \sigma_b} \left[\varepsilon_2 - i \frac{(\sigma_a + \sigma_b)\eta_0}{k_0 d} \right] \right\}}, \tag{3.21}$$

For the simple case of $\varepsilon_2 = 1$ *and* $\sigma_a = \sigma_b = \sigma$, the eq. (3.20) lead to

$$\beta / k_o \simeq \sqrt{1 - i \frac{2}{\sigma \eta_o k_o d}}. \tag{3.22}$$

3.4 Power Flowing Within The PPWG Graphene (TM Mode)

The power flow in the structure is defined as mentioned in chapter 2:

$$P_{total} = \frac{\beta}{2\omega} \int_{-\infty}^{\infty} \frac{|H_y(x)|^2}{\varepsilon(x)} dx ; \tag{3.23}$$

$$P_{TMtotal} = P_1 + P_2 + P_3 . \tag{3.24}$$

Substituting for $H_y(x)$ form Eq. (3.6) into Eq. (3.14), we get:

$$P_1 = -i \frac{\beta A^2}{4\omega \varepsilon_0 \varepsilon_1 \gamma_1} e^{-i\gamma_1 d}, \tag{3.25a}$$

$$P_2 = \frac{\beta}{4\omega \varepsilon_0 \varepsilon_2} \left[\left(B^2 + C^2 \right) d - \left(B^2 - C^2 \right) \cdot \frac{\sin(\gamma_2 d)}{\gamma_2} \right], \tag{3.25b}$$

$$P_3 = -i \frac{\beta D^2}{4\omega \varepsilon_0 \varepsilon_3 \gamma_3} e^{-i\gamma_3 d}. \tag{3.25c}$$

Then

$$P_{TMtotal} = -\frac{\beta}{4\omega\varepsilon_0}\left\{ i\left(\frac{A^2 e^{-i\gamma_1 d}}{\varepsilon_1\gamma_1} + \frac{D^2 e^{-i\gamma_3 d}}{\varepsilon_3\gamma_3}\right) - \frac{\left(B^2 + C^2\right)}{\varepsilon_2} d + \left(B^2 - C^2\right)\cdot\frac{\sin(\gamma_2 d)}{\varepsilon_2\gamma_2}\right\}. \tag{3.26}$$

The coefficients *A, B, C* and *D* are related to each other through the equations:

$$B = A\left\{\left(1+\frac{\sigma_a\gamma_1}{\omega\varepsilon_1\varepsilon_0}\right)\cdot\sin(\gamma_2 d/2) - i\left(\frac{\varepsilon_2\gamma_1}{\varepsilon_1\gamma_2}\right)\cdot\cos(\gamma_2 d/2)\right\}\cdot e^{-i\gamma_1 d/2}, \tag{3.27}$$

$$C = A\left\{\left(1+\frac{\sigma_a\gamma_1}{\omega\varepsilon_1\varepsilon_0}\right)\cdot\cos(\gamma_2 d/2) + i\left(\frac{\varepsilon_2\gamma_1}{\varepsilon_1\gamma_2}\right)\cdot\sin(\gamma_2 d/2)\right\}\cdot e^{-i\gamma_1 d/2}, \tag{3.28}$$

$$D = A\,\frac{\left\{\left(1+\frac{\sigma_a\gamma_1}{\omega\varepsilon_1\varepsilon_0}\right)\cdot\cos(\gamma_2 d/2) + i\left(\frac{\varepsilon_2\gamma_1}{\varepsilon_1\gamma_2}\right)\cdot\sin(\gamma_2 d/2)\right\}\cdot e^{-i\gamma_1 d/2}}{\left\{\left(1+\frac{\sigma_b\gamma_3}{\omega\varepsilon_3\varepsilon_0}\right)\cdot\cos(\gamma_2 d/2) + i\left(\frac{\varepsilon_2\gamma_3}{\varepsilon_3\gamma_2}\right)\cdot\sin(\gamma_2 d/2)\right\}\cdot e^{-i\gamma_3 d/2}}, \tag{3.29}$$

For sensing applications, the most important parameter for optical waveguide sensor is the fraction of total power flowing in the upper [88]:

$$S_{TM} = \frac{P_1}{P_{total}}, \tag{3.30}$$

$$= \frac{A^2 e^{-i\gamma_1 d}}{\varepsilon_1\gamma_1\left\{ i\left(\frac{A^2 e^{-i\gamma_1 d}}{\varepsilon_1\gamma_1} + \frac{D^2 e^{-i\gamma_3 d}}{\varepsilon_3\gamma_3}\right) - \frac{(B^2 + C^2)}{\varepsilon_2} d + (B^2 - C^2)\cdot\frac{\sin(\gamma_2 d)}{\varepsilon_2\gamma_2}\right\}}. \tag{3.31}$$

3.5 Numerical Results

The following results are for the TM mode of a graphene PPWG. For simplicity, suspended graphene sheets will be assumed ($\varepsilon_1 = \varepsilon_2 = \varepsilon_3 = 1$) to avoid any influence of a dielectric substrate (remote phonon scattering , opening of a band gap, etc.), the chemical potential is μ_c= 0.5eV, which leads to a large charge density n= 2×10^{13} cm^{-2}. Since μ_c/k_BT >>1 thought at least 500 K, for all temperatures of interest the conductivity is

$$\sigma \simeq -i\,\frac{e^2\mu_c}{\pi\hbar(\omega - i\,\tau^{-1})}. \tag{3.32}$$

Therefore, the following results are only dependent on temperature via the relaxation time τ. The relaxation time depends on a variety of other factors, including the presence of impurities, and for simplicity here we use a constant value of τ =5 × 10^{-13} s (Note: the values of μ and τ are in the range of values considered in Ref. 65).

Furthermore, assuming that μ_c/k_BT >> 1, at higher frequencies (ω >> τ^{-1}) the only control over the conductivity is via the chemical potential.

For lower frequencies(ω <<τ^{-1}),

$$\sigma \simeq \frac{e^2\mu_c\tau}{\pi\hbar}. \tag{3.33}$$

and the conductivity is controlled by the product $\mu_c\tau$.

Fig (3.2) shows the complex effective index β/k_0 from eq. (3.18) of the graphene PPWG with plate separation d=100 nm, for frequencies in the GHz/far-infrared range. The upper and lower dash curves are for dispersion relation eq. (3.18), the dash dot curves are the approximation one, showing excellent agreement with the numerical solution of Eq. (3.21).

The conductivity curves are marked by solid and dot lines. It can be seen that throughout most of the considered frequency range, the TM mode is relatively nondispersive, even though the conductivity itself is moderately dispersive.

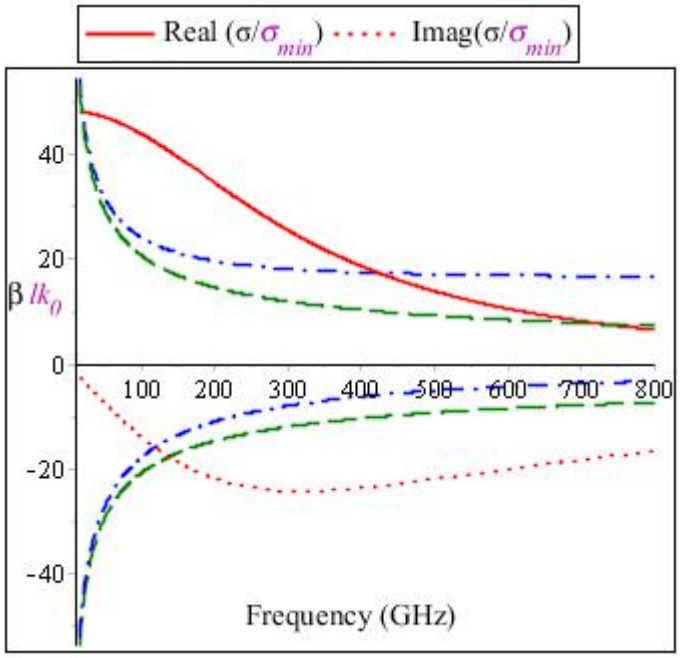

Fig. 3.2. The dash line is effective index β/k_0 from Eq. (3.18) for a graphene PPWG with d=100nm. The approximation Eq. (3.21) is shown as blue dash dot lines. The conductivity is normalized by $\sigma_{min} = \pi e^2/2h$ [87].

Fig (3.3) shows effective index β/k_0 of the graphene PPWG versus the frequencies of the dielectric layer for different values of the thickness. As the thickness of dielectric layer increases, the real part of the normalized phase constant β/k_0 is decreasing. Additionally, with increasing the frequency, the real part of the effective index β/k_0 decreases; this because the real part of graphene conductivity decreases with the frequency, as shown in the figure (3.2). While the imaginary part of effective index β/k_0 increases with increasing the operating frequency; because the imaginary part of conductivity increases with the frequency as shown in the same figure (3.2).

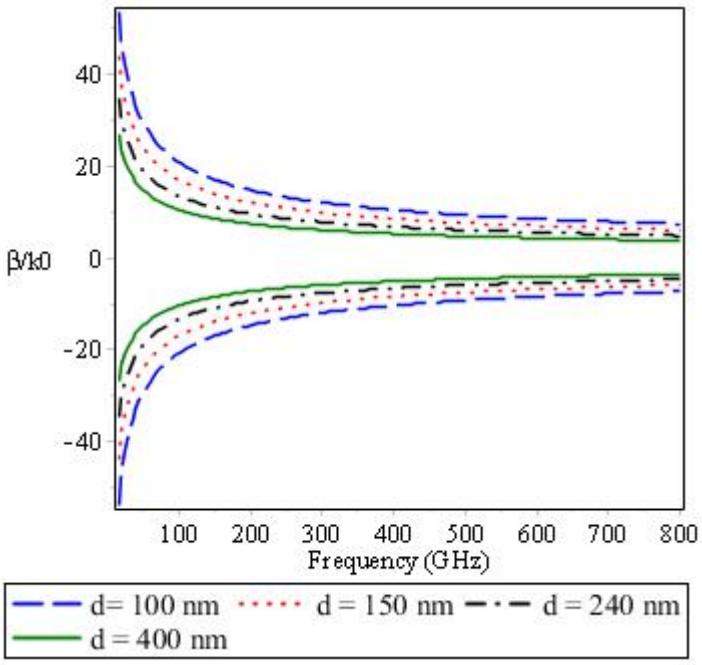

Fig. 3.3. The effective index β/k_0 versus the frequencies of the dielectric layer for different values of the thickness.

Fig (3.4) shows the effective index β/k_0 of the graphene PPWG with versus the thickness of the dielectric layer for different values of the frequency. As the frequency of dielectric layer increases, the real part of the effective index β/k_0 is decreasing. Additionally, with increasing the thickness, the real part of the normalized phase constant β/k_0 decreases; this because the real part of graphene conductivity decreases with the frequency, as shown in the figure (3.2). While the imaginary part of effective index β/k_0 increase with increasing thickness; because the imaginary part of conductivity increases with the frequency as shown in the same figure (3.2).

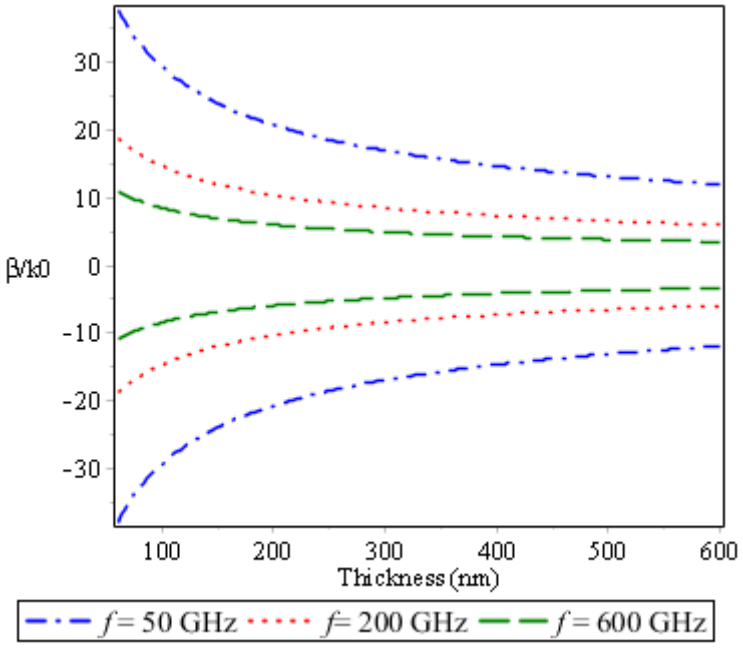

Fig. 3.4. The effective index β/k_0 versus the thickness of the dielectric layer for different values of the frequencies.

Figure 3.5 and 3.6 show the variation of the real and imaginary parts of the sensitivity of the proposed sensor with the thickness dielectric guiding layer for different values of frequencies. It can be seen from the figure 3.5, the sensitivity is positive, but in figure 3.6, the sensitivity is negative. The absolute values of the real and imaginary parts of the sensitivity increases as f increases.

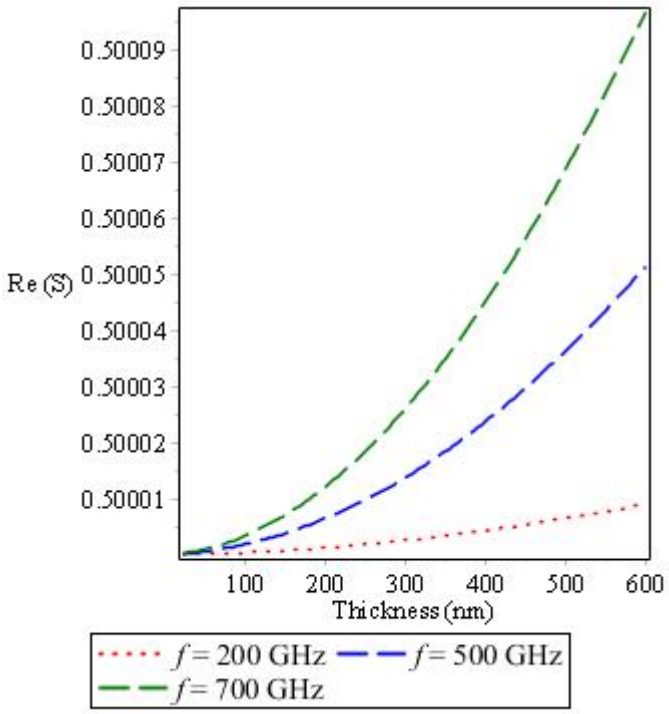

Fig.3.5.The real part of the sensitivity of the proposed sensor versus the thickness of the dielectric layer for different values of the frequencies.

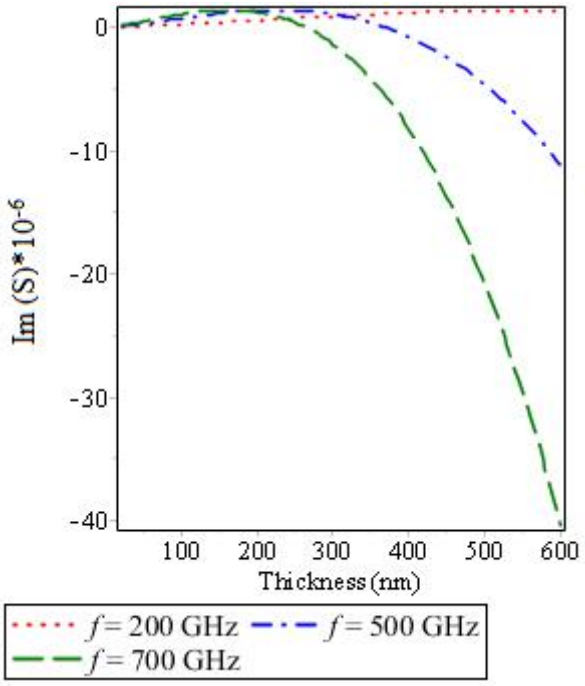

Fig.3.6. The imaginary part of the sensitivity of the proposed sensor versus the thickness of the dielectric layer for different values of the frequencies.

Figure 3.7 and 3.8 show the variation of the real and imaginary parts of the sensitivity of the proposed sensor with the frequency dielectric guiding layer for different values of thickness. It can be seen from the figures the sensitivity is positive.

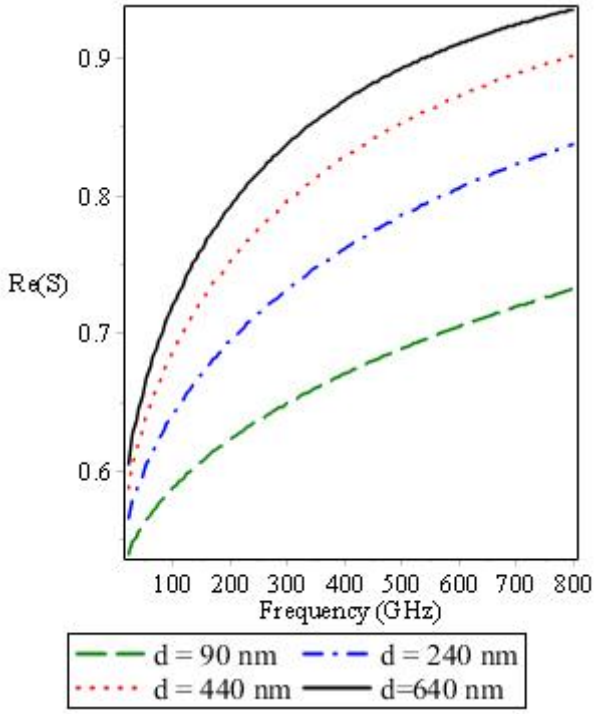

Fig. 3.7. The real part of the sensitivity of the proposed sensor versus the frequency operating of the dielectric layer for different values of the Thickness.

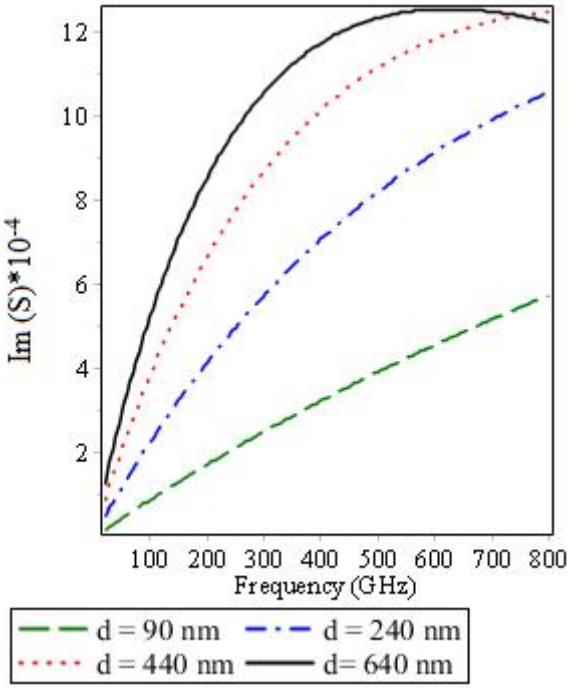

Fig. 3.8. The imaginary part of the sensitivity of the proposed sensor versus the frequency operating of the dielectric layer for different values of the Thickness.

CHAPTER FOUR

Electromagnetic Waves at Graphene Parallel-Plate waveguide (TE-Mode)

In this chapter, we examine the electromagnetic waves at graphene parallel-plate of TE polarized wave, found the dispersion relation, applied G. Hansson approximation, calculate the total power flow through Graphene-PPWG, and the sensitivity of the proposed sensor will be presented.

4.1 Structure Analysis

In Fig. 3.1 a schematic of the graphene Parallel-plate is presented. In this section we will discuss the TE (s-polarized) mode.

4.2 The Dispersion Relation

We consider the TE wave with the magnetic filed perpendicular to the plane of incidence (*xz*), possesses the electromagnetic field components **E** = {0, E_y, 0}, ***H***= {H_x, 0, H_z}.

Maxwell's equations require that in the $E_y(x)$ introduced in eq. (3.1) satisfies:

$$\frac{\partial^2}{\partial x^2} E_y(x) + (k_j{}^2 - \beta^2) E_y(x) = 0. \tag{4.1}$$

Where $k_j = k_j = \sqrt{\varepsilon_j}\, k_o$, $j = 1,2,3$ is the wavenumber in region, j, ε_j is the relative permittivity of region j, and $k_o = \omega\sqrt{\mu_o \varepsilon_o} = \omega/c$ is the free-space wavenumber (c is the speed of light in vacuum).

The waveguiding axis is chosen as the z-axis, and from source- free Maxell's equations the TE^z fields in each region are:

$$\frac{\partial E_y}{\partial z} = i\,\omega\mu_j\,\mu_0 H_x\,, \tag{4.2a}$$

$$\frac{\partial E_y}{\partial x} = -i\,\omega\mu_j\,\mu_0 H_z\,, \tag{4.2b}$$

$$\frac{\partial H_x}{\partial z} - \frac{\partial H_z}{\partial x} = -i\,\omega\mu_0 E_y\,, \tag{4.2c}$$

Modal fields are

$$E_y(x) = \begin{cases} A e^{-i\gamma_1 x}, & x > d/2 \\ B\sin(\gamma_2 x) + C\cos(\gamma_2 x) & -d/2 \le x \le d/2, \\ D e^{i\gamma_3 x} & x < -d/2 \end{cases} \tag{4.3}$$

$$H_z(x) = \begin{cases} \dfrac{A\gamma_1}{\omega\mu_0\mu_1} e^{-i\gamma_1 x} & x > d/2 \\ i\,\dfrac{\gamma_2}{\omega\mu_0\mu_2}\left[B\cos(\gamma_2 x) - C\sin(\gamma_2 x)\right] & -d/2 \le x \le d/2 \\ -\dfrac{D\gamma_3}{\omega\mu_0\mu_3} e^{i\gamma_3 x} & x < -d/2 \end{cases} \tag{4.4}$$

Where *A, B,C* and *D* are constants with respect to position.

By applied Boundary Conditions (3.5 -3.6):

(1) At x = d/2,

$$H_y^{(1)} - H_y^{(2)} = -\sigma_a E_z^{(1)},$$

$$\frac{A\gamma_1}{\omega\mu_0\mu_1} e^{-i\gamma_1 d/2} - i\,\frac{\gamma_2}{\omega\mu_0\mu_2}\left[B\cos(\gamma_2 d/2) - C\sin(\gamma_2 d/2)\right] = -\sigma_a A e^{-i\gamma_1 d/2},$$

$$\left[B\cos(\gamma_2 d/2) - C\sin(\gamma_2 d/2)\right] = -iA\left(\frac{\gamma_1\mu_2}{\gamma_2\mu_1}\right)\left(1 + \frac{\omega\mu_0\mu_1\sigma_a}{\gamma_1}\right) e^{-i\gamma_1 d/2}, \tag{4.5}$$

$$E_z^{(1)} - E_z^{(2)} = 0,$$
$$A e^{-i\gamma_1 d/2} = B \sin(\gamma_2 d/2) + C \cos(\gamma_2 d/2), \tag{4.6}$$

From eq.(4.5) and eq.(4.6) we have get:

$$B = -C \frac{\left[\cos(\gamma_2 d/2) + i c_a \sin(\gamma_2 d/2)\right]}{\left[\sin(\gamma_2 d/2) - i c_a \cos(\gamma_2 d/2)\right]}, \tag{4.7}$$

Where

$$c_a = \left(\frac{\mu_1 \gamma_2}{\mu_2 \gamma_1}\right)\left(1 + \frac{\omega \mu_1 \mu_0 \sigma_a}{\gamma_1}\right)^{-1}, \tag{4.8}$$

(2) At x = -d/2,

$$H_y^{(2)} - H_y^{(3)} = -\sigma_b E_z^{(3)},$$
$$\frac{i\gamma_2}{\omega \mu_0 \mu_3}\left[B \cos(\gamma_2 d/2) + C \sin(\gamma_2 d/2)\right] - \left(-\frac{D\gamma_3}{\omega \varepsilon_0 \varepsilon_3}\right) D e^{-i\gamma_3 d/2} = -\sigma_b D e^{-i\gamma_3 d/2},$$
$$B \cos(\gamma_2 d/2) + C \sin(\gamma_2 d/2) = i\left(\frac{\gamma_3 \mu_2}{\gamma_2 \mu_3}\right)\left(1 + \frac{\omega \mu_0 \mu_3 \sigma_b}{\gamma_3}\right) D e^{-i\gamma_3 d/2}, \tag{4.9}$$

$$E_z^{(2)} - E_z^{(3)} = 0,$$
$$\left[B \sin(-\gamma_2 d/2) + C \cos(-\gamma_2 d/2)\right] = D e^{-i\gamma_3 d/2},$$
$$-B \sin(\gamma_2 d/2) + C \cos(\gamma_2 d/2) = D e^{-i\gamma_3 d/2}, \tag{4.10}$$

From eq.(4.9) and eq.(4.10) we have get:

$$B = -C \frac{\left[\cos(\gamma_2 d/2) + i c_b \sin(\gamma_2 d/2)\right]}{\left[-\sin(\gamma_2 d/2) + i c_b \cos(\gamma_2 d/2)\right]}, \tag{4.11}$$

Where

$$c_b = \left(\frac{\mu_3\gamma_2}{\mu_2\gamma_3}\right)\left(1+\frac{\omega\mu_3\mu_0\sigma_b}{\gamma_3}\right)^{-1}, \tag{4.12}$$

By solving eq. (4.7) with eq.(4.11) and using Applications of Trigonometric, we have the dispersion equation for the guided modes:

$$\left(c_a + c_b\right)\cos\gamma_2 d + i\left(1+c_a c_b\right)\sin\gamma_2 d = 0, \tag{4.13}$$

and $\gamma_j^2 = k_j^2 - \beta^2$

Eq. (4.13) can be write as:

$$\tan\gamma_2 d = \frac{\left(c_a + c_b\right)}{\left(c_a c_b + 1\right)}. \tag{4.14}$$

4.3 Approximation Solution

Hanson assumed the approximation at TM mode case, similarly we apply the Hanson approximation to found out the approximation solution[87].

The approximation is:

$$\tan\gamma_2 d \approx \gamma_2 d, \quad \frac{\sigma_a\omega\mu_o}{\gamma_1}, \frac{\sigma_b\omega\mu_o}{\gamma_3} \gg 1, \tag{4.15}$$

Where $\mu_1 = \mu_2 = \mu_3 = 1.$

When we applied this approximation at eq. (4.6), we obtain

$$\beta / k_o = \sqrt{\varepsilon_2 + \eta_o^2\sigma_a\sigma_b\left[1 - i\,\frac{\left(\sigma_a + \sigma_b\right)}{\eta_o k_o d\,\sigma_a\sigma_b}\right]}, \tag{4.16}$$

For the simple case of $\varepsilon_2 = 1$ *and* $\sigma_a = \sigma_b = \sigma$, the eq. (4.8) lead to [89-91]:

$$\beta / k_o \simeq \sqrt{1 - i\,\frac{2\sigma\eta_o}{k_o d}}. \tag{4.17}$$

4.4 Power Flowing Within The PPWG Graphene (TM Mode)

The power flow in the structure is defined as in Chapter 2 :

$$P_{total} = \frac{\beta}{2\omega}\int_{-\infty}^{\infty}\frac{\left|E_y(x)\right|^2}{\mu(x)}dx\,; \tag{4.18}$$

$$P_{TEtotal} = P_1 + P_2 + P_3\,. \tag{4.19}$$

Substituting for $E_y(x)$ form Eq. (4.12) into Eq. (3.13), we get:

$$P_1 = -i\,\frac{\beta A^2}{4\omega\mu_0\gamma_1}e^{-i\gamma_1 d}, \tag{4.20a}$$

$$P_2 = \frac{\beta}{4\omega\mu_0}\left[\left(B^2 + C^2\right)d - \left(B^2 - C^2\right)\cdot\frac{\sin(\gamma_2 d)}{\gamma_2}\right], \tag{4.20b}$$

$$P_3 = -i\,\frac{\beta D^2}{4\omega\mu_0\gamma_3}e^{i\gamma_3 d}. \tag{4.20c}$$

then,

$$P_{TEtotal} = -\frac{\beta}{4\omega\mu_0}\left\{i\left(\frac{A^2 e^{-i\gamma_1 d}}{\gamma_1} + \frac{D^2 e^{-i\gamma_3 d}}{\gamma_3}\right) - \left(B^2 + C^2\right)d + \left(B^2 - C^2\right)\cdot\frac{\sin(\gamma_2 d)}{\gamma_2}\right\}. \tag{4.21}$$

The coefficients *A, B, C* and *D* are related to each other through the equations:

$$B = A\left\{\sin(\gamma_2 d/2) - i\left(\frac{\gamma_1}{\gamma_2}\right)(1+\frac{\omega\mu_0\sigma_a}{\gamma_1})\cdot\cos(\gamma_2 d/2)\right\}\cdot e^{-i\gamma_1 d/2}, \tag{4.22}$$

$$C = A\left\{\cos(\gamma_2 d/2) + i\left(\frac{\gamma_1}{\gamma_2}\right)(1+\frac{\omega\mu_0\sigma_a}{\gamma_1})\sin(\gamma_2 d/2)\right\}\cdot e^{-i\gamma_1 d/2}, \tag{4.23}$$

$$D = A\frac{\left\{\sin(\gamma_2 d/2) - i\left(\frac{\gamma_1}{\gamma_2}\right)(1+\frac{\omega\mu_0\sigma_a}{\gamma_1})\cdot\cos(\gamma_2 d/2)\right\}\cdot e^{-i\gamma_1 d/2}}{\left\{\sin(\gamma_2 d/2) - i\left(\frac{\gamma_3}{\gamma_2}\right)(1+\frac{\omega\mu_0\sigma_b}{\gamma_3})\cdot\cos(\gamma_2 d/2)\right\}\cdot e^{-i\gamma_3 d/2}}, \tag{4.24}$$

The sensitivity is:

$$S_{TE} = \frac{P_1}{P_{total}}, \tag{4.25}$$

$$= \frac{A^2 e^{-i\gamma_2 d}}{\gamma_1\left\{\left(\frac{A^2 e^{-i\gamma_2 d}}{\gamma_1} + \frac{D^2 e^{-i\gamma_3 d}}{\gamma_3}\right) - \left(B^2 + C^2\right)d + \left(B^2 - C^2\right)\cdot\frac{\sin(\gamma_2 d)}{\gamma_2}\right\}}. \tag{4.26}$$

4.5 Numerical Results

Fig (4.1) shows the effective index constant β/k_0 from eq. (4.13) of the graphene PPWG with plate separation d=100 μm, for the operating frequency in the GHz/far-infrared range. The upper and lower dash curves are for dispersion relation eq. (4.13), the dash dot curves are the approximation one, showing excellent agreement with the numerical solution of Eq. (4.16). The conductivity curves are marked by solid and dot red lines.

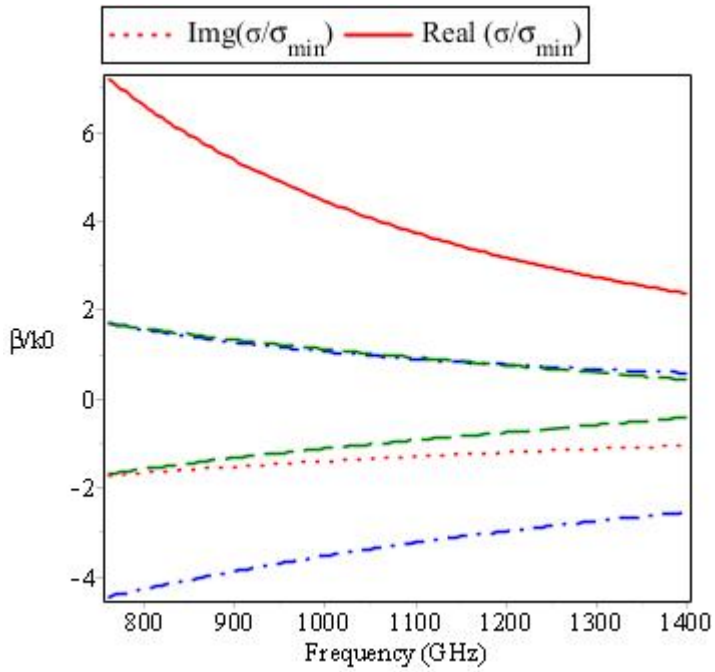

Fig. 4.1. The dash line is effective index β/k_0 from Eq. (4.13) for a graphene PPWG with d=100μm. The approximation Eq. (4.16) is shown as blue dash dot lines. The conductivity is normalized by $\sigma_{min} = \pi e^2/2h$.

Fig (4.2) shows the effective index β/k_0 of the graphene PPWG versus the frequencies for different values of the thickness. As the thickness of dielectric layer increases, the real part of the effective index β/k_0 decreases. Additionally, with increasing frequency, the real part of the effective index β/k_0 decreases; this because the real part of graphene conductivity decreases with the frequency, as shown in the figure (4.1). While the imaginary part of the effective index β/k_0 increases with increasing frequency.

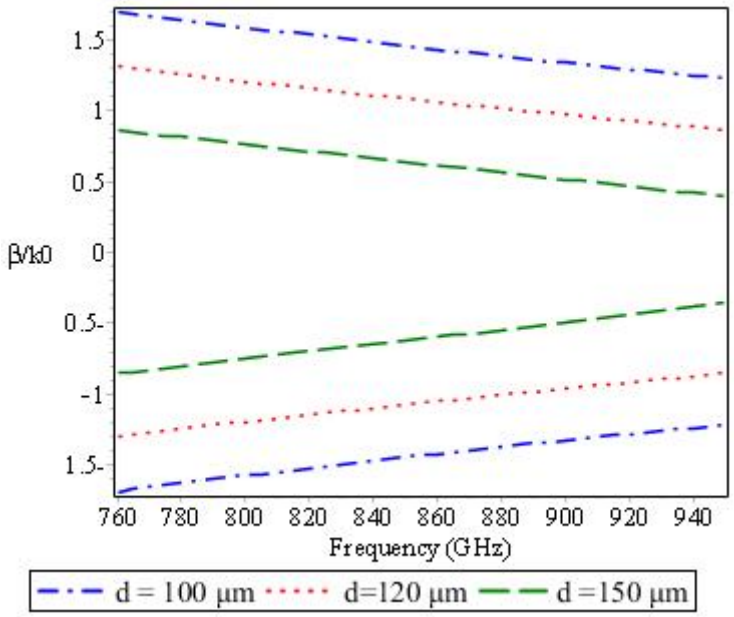

Fig. 4.2. The effective index β/k_0 versus the frequencies of the dielectric layer for different values of the thickness.

Fig (4.3) shows the effective index β/k_0 of the graphene PPWG versus the thickness for different values of the frequency. As the frequency of dielectric layer increases, the effective index β/k_0 decreases. Additionally, with increasing thickness, the real part of the effective index β/k_0 decreases. While the imaginary part of the effective index β/k_0 increases with increasing thickness.

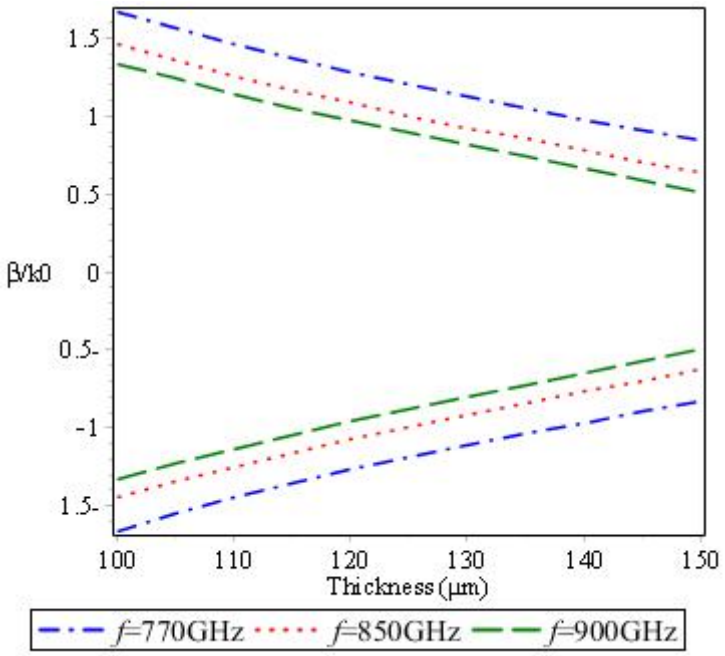

Fig. 4.3. **The effective index β/k_0 versus the thickness of the dielectric layer for different values of the frequencies.**

Figure 4.4 and 4.5 show the variation of the real and imaginary parts of the sensitivity of the proposed sensor with the thickness dielectric guiding layer for different values of frequencies. It can be seen from the figure 4.4, the sensitivity is positive, but in figure 4.5, the sensitivity is negative. The first peak appear when the thickness d=158μm at frequency *f*=770GHz. Additionally the absolute values of the real and imaginary parts of the sensitivity decrease as the frequency increases.

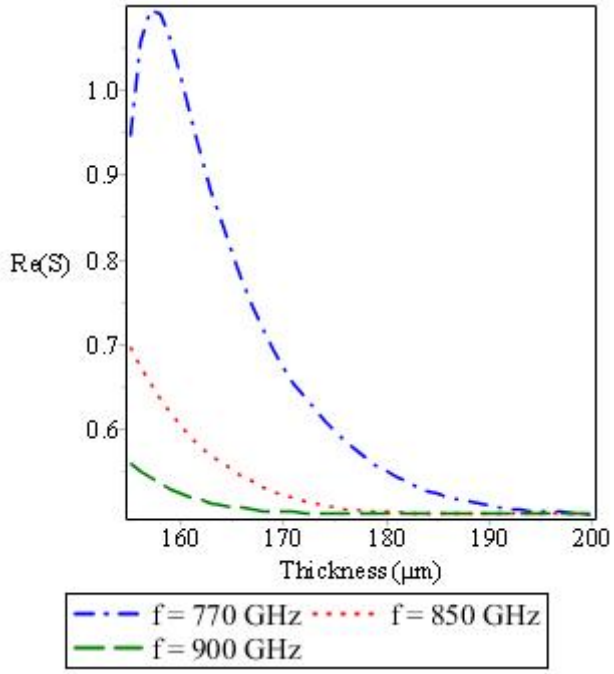

Fig. 4.4. The real part of the sensitivity of the proposed sensor versus the thickness of the dielectric layer for different values of the frequencies.

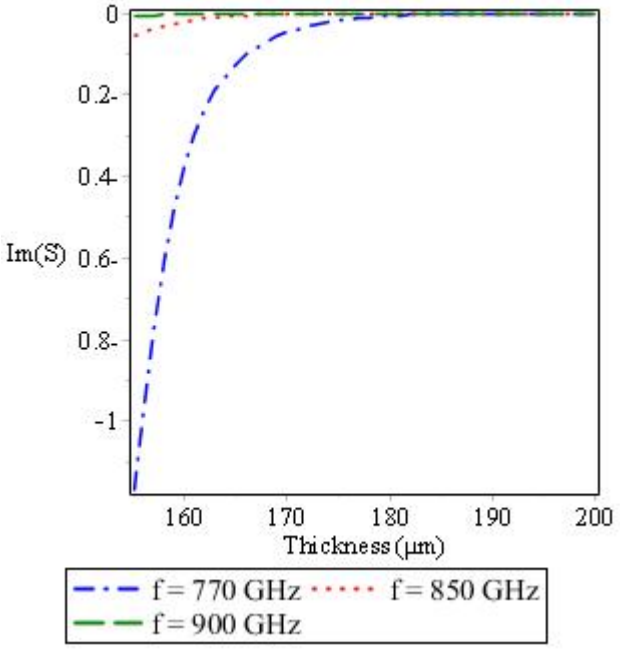

Fig. 4.5. The imaginary part of the sensitivity of the proposed sensor versus the thickness of the dielectric layer for different values of the frequencies.

Figure 4.6 and 4.7 show the variation of the real and imaginary parts of the sensitivity of the proposed sensor with the frequency dielectric guiding layer for different values of thickness.

Figure 4.6, shows many behaviour of sensitivity with a difference value of thickness. At the first value of thickness (d = 100μm) the sensitivity is start from the origin, then decreasing with increase values of frequency f. When d=150μm the sensitivity increases and becomes positive, it has peak at a specific value of frequency(f = 818 GHz) and is decreasing again. when d =200 μm the sensitivity is very weak and stable. Figure 4.7 shows the sensitivity is negative at all values of d.

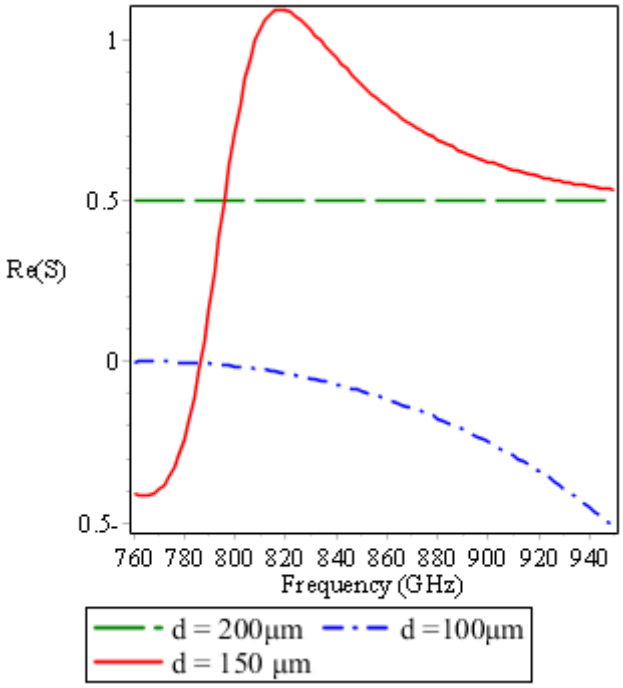

Fig. 4.6. The real part of the sensitivity of the proposed sensor versus the frequencies of the dielectric layer for different values of the Thickness.

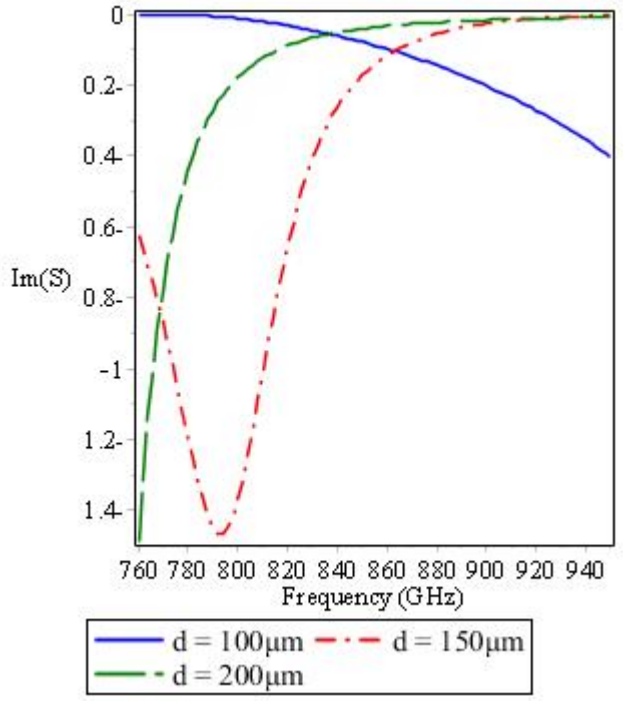

Fig. 4.7. The imaginary part of the sensitivity of the proposed sensor versus the frequencies of the dielectric layer for different values of the Thickness.

CHAPTER FIVE

Sensitivity at Graphene Left-hand-Martial Waveguide Structure: (TM Case)

In this chapter, a three-layer planar waveguide consisting of parallel plate of graphene, a thin left handed material medium layer is under consideration. We examine the electromagnetic waves at (graphene – LHM) of TM mode, and find out the dispersion relation, sensitivity of Graphene-LHM-Graphene Structure. Moreover, the total power flowing for each layers will be presented and will be compared to Right handed material waveguide sensor.

5.1 Structure Analysis

In this section, we consider a LHM thin film of thickness d occupying the region $x = -d/2$ and $x = d/2$ and infinite in y and z directions, which is characterized by an electric permittivity ε_2 and magnetic permeability μ_2. This film is sandwiched between two semi-infinite graphene layers occupying the regions $x < -d/2$ and $x > d/2$ and having parameters (ε_1 , μ_1) and (ε_3 , μ_3), respectively.

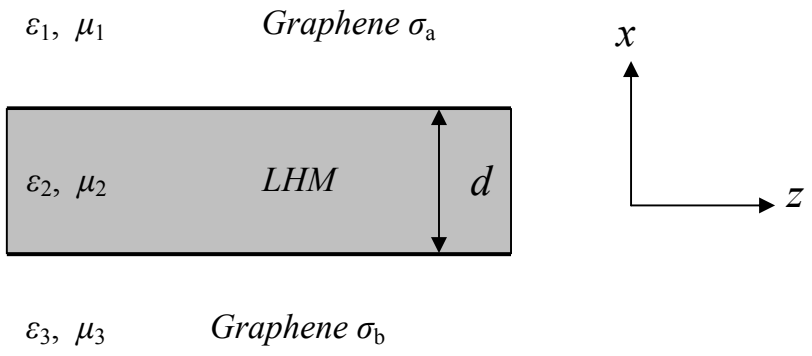

Figure 5.1: Left-Handed Material Layer sandwiched between two Graphene Sheets.

5.2 The Dispersion Relation of Graphene –LHM (TM-Mode):

The magnetic profiles in the structure region are:

$$H_y(x)=\begin{cases} A e^{-\gamma_1 x}, & x > d/2 \\ B\sin\gamma_2 x + C\cos\gamma_2 x & -d/2 \le x \le d/2 \\ De^{\gamma_3 x} & x < -d/2 \end{cases}. \tag{5.1}$$

The dispersion equation is obtained in similar way as mentioned in the Ch. (3):

$$(c_a + c_b)\cos\gamma_2 d - (1 - c_a c_b)\sin\gamma_2 d = 0. \tag{5.2}$$

where

$$c_a = \left(\frac{\varepsilon_2\gamma_1}{\varepsilon_1\gamma_2}\right)\left(1 - i\,\frac{\sigma_a\gamma_1}{\omega\varepsilon_1\varepsilon_0}\right)^{-1}, \tag{5.3}$$

$$c_b = \left(\frac{\varepsilon_2\gamma_3}{\varepsilon_3\gamma_2}\right)\left(1 - i\,\frac{\sigma_b\gamma_3}{\omega\varepsilon_3\varepsilon_0}\right)^{-1}, \tag{5.4}$$

and $\gamma_j^2 = k_j^2 - \beta^2$.

Taking into account some differences in the new notations k_j ($k_j = \sqrt{\varepsilon_j \mu_j}\,k_0$, $i = 1, 2, 3$), where μ_i have a value (not equal 1).

Eq, (5.2) can be rewritten as:

$$\tan\gamma_2 d = \frac{c_a + c_b}{1 - c_a c_b}. \tag{5.5}$$

5.3 Power flowing within the PPWG graphene (TM mode):

The power flow in the structure is:

$$P_{total} = \frac{\beta}{2\omega}\int_{-\infty}^{\infty}\frac{\left|H_y(x)\right|^2}{\varepsilon(x)}dx; \tag{5.6}$$

$$P_{TMtotal} = P_1 + P_2 + P_3. \tag{5.7}$$

Substituting for $H_y(x)$ form Eq. (5.1) into Eq. (5.6), we get:

$$P_1 = -\frac{\beta A^2}{4\omega\varepsilon_0\varepsilon_1\gamma_1}e^{\gamma_1 d} \tag{5.8a}$$

$$P_2 = \frac{\beta}{4\omega\varepsilon_0\varepsilon_2}\left[\left(B^2+C^2\right)d - \left(B^2-C^2\right)\cdot\frac{\sin(\gamma_2 d)}{\gamma_2}\right] \tag{5.8b}$$

$$P_3 = -\frac{\beta D^2}{4\omega\varepsilon_0\varepsilon_3\gamma_3}e^{-\gamma_3 d} \tag{5.8c}$$

Then

$$P_{TMtotal} = -\frac{\beta}{4\omega\varepsilon_0}\left\{\left(\frac{A^2e^{\gamma_1 d}}{\varepsilon_1\gamma_1}+\frac{D^2e^{\gamma_3 d}}{\varepsilon_3\gamma_3}\right) - \frac{\left(B^2+C^2\right)}{\varepsilon_2}d + \left(B^2-C^2\right)\cdot\frac{\sin(\gamma_2 d)}{\varepsilon_2\gamma_2}\right\}. \tag{5.9}$$

The coefficients *A, B, C* and *D* are related to each other through the equations:

$$B = A\left\{\left(1 - i\,\frac{\sigma_a\gamma_1}{\omega\varepsilon_1\varepsilon_0}\right)\cdot\sin(\gamma_2 d/2) - \left(\frac{\varepsilon_2\gamma_1}{\varepsilon_1\gamma_2}\right)\cdot\cos(\gamma_2 d/2)\right\}\cdot e^{-\gamma_1 d/2}, \tag{5.10}$$

$$C = A\left\{\left(1 + i\,\frac{\sigma_a\gamma_1}{\omega\varepsilon_1\varepsilon_0}\right)\cdot\cos(\gamma_2 d/2) + \left(\frac{\varepsilon_2\gamma_1}{\varepsilon_1\gamma_2}\right)\cdot\sin(\gamma_2 d/2)\right\}\cdot e^{-\gamma_1 d/2}, \tag{5.11}$$

$$D = A\frac{\left\{\left(1+i\,\frac{\sigma_a\gamma_1}{\omega\varepsilon_1\varepsilon_0}\right)\cdot\cos(\gamma_2 d\ /2)+\left(\frac{\varepsilon_2\gamma_1}{\varepsilon_1\gamma_2}\right)\cdot\sin(\gamma_2 d\ /2)\right\}\cdot e^{-\gamma_1 d/2}}{\left\{\left(1+i\,\frac{\sigma_b\gamma_3}{\omega\varepsilon_3\varepsilon_0}\right)\cdot\cos(\gamma_2 d\ /2)+\left(\frac{\varepsilon_2\gamma_3}{\varepsilon_3\gamma_2}\right)\cdot\sin(\gamma_2 d\ /2)\right\}\cdot e^{-\gamma_3 d/2}}, \tag{5.12}$$

The sensitivity is:

$$S_{TM_{LHM}} = \frac{P_1}{P_{total}}, \tag{5.13}$$

$$= \frac{A^2 e^{\gamma_1 d}}{\varepsilon_1\gamma_1\left\{\left(\frac{A^2 e^{\gamma_1 d}}{\varepsilon_1\gamma_1}+\frac{D^2 e^{\gamma_3 d}}{\varepsilon_3\gamma_3}\right)-\frac{(B^2+C^2)d}{\varepsilon_2}+(B^2+C^2)d\cdot\frac{\sin(\gamma_2 d)}{\varepsilon_2\gamma_2}\right\}}. \tag{5.14}$$

5.4Numerical results

In our analysis, we have considered two laterally infinite graphene sheets spaced a distance d apart with $\varepsilon_1 = \varepsilon_3 = 1$ and $\mu_1 = \mu_3 = 1$. The LHM layer is sandwiched between a graphene sheets occupies the region x > d/2 with $\varepsilon_1 = \mu_1 = 1$, and the region x < -d/2 with $\varepsilon_3 = \mu_3 = 1$.

Also, in this section, we graph the Right Handed Materials (RHM), which is a material ε_2 and μ_2 have a positive values.

Fig 5.2 and 5.3 show the real and the imaginary parts of the effective index ($n_{eff} = \beta/k_0$) from eq. (5.5) of LHM layer with plate separation d=100 nm, for frequencies in the THz frequency. Its clear the product of ε_2 and $\mu_2 = 4.0$.

We noted when $\varepsilon_2 = -4$, $\mu_2 = -1$, the effective index has a highest value ($n_{eff} = 4.4$), when $\varepsilon_2 = -1$, $\mu_2 = -4$, the effective index has a lowest value ($n_{eff} = 2.6$), when $\varepsilon_2 = \mu_2 = -2$, we have the a value ($n_{eff} = 3.3$).

At the same curve, we plot the RHM at THz region. In Figs. 5.2, we assumed a RHM film $\varepsilon_2 = 1$, $\mu_2 = 1$.

As we see, the effective index n_{eff} of RHM layer is less than that of a LHM layer. This behavior of the effective refractive index can be attributed to following argument. The effective refractive index of a propagating mode is determined by the thickness of the guiding layer and constitutive parameters of the materials constituting the waveguide. For a constant guiding layer thickness, it depends solely on the graphene permittivity and magnetic permeability of the media constituting the waveguide, but these values are equals for LHM and RHM materials.

On other hand, the effective index n_{eff} decreases as the frequency increases as shown in Fig. 5.2, and 5.3 for LHM, but for RHM the real part has the same behavior, but the imaginary part of the n_{eff} increases as the frequency as shown in Fig. 5.3.

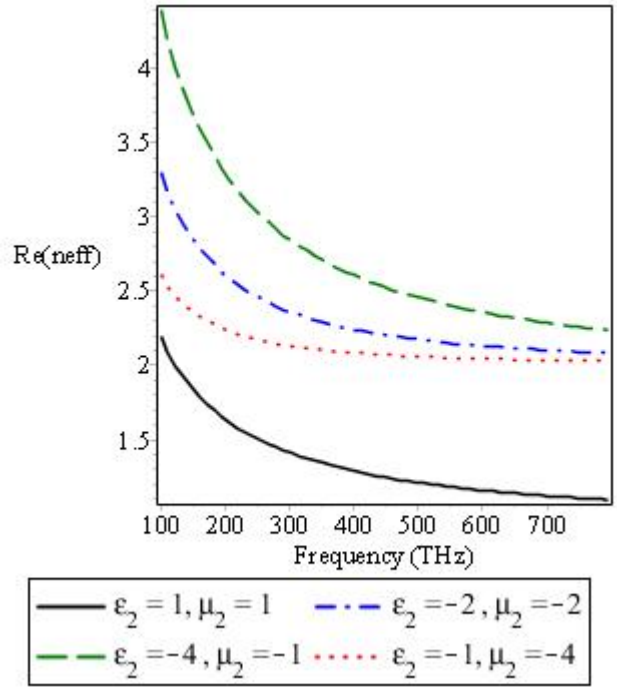

Fig. 5.2. The real part of the effective index n_{eff} from Eq. from Eq. (5.2) versus the frequency of the guiding layer for different values of the core permittivity and permeability for LHM and RHM with d=100nm. The conductivity is normalized by $\sigma_{min} = \pi e^2/2h$.

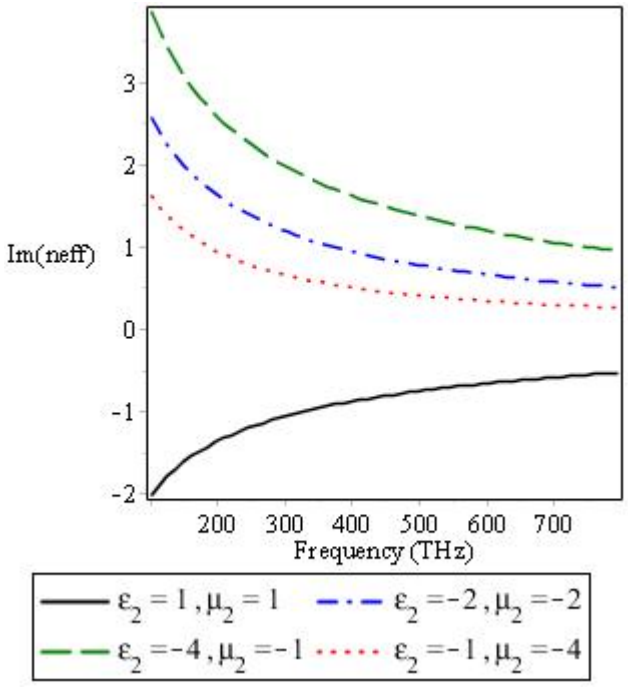

Fig. 5.3 The imaginary part of n_{eff} from Eq. (5.2) versus the frequency of the guiding layer for different values of the core permittivity and permeability for LHM and RHM with d=100nm . The conductivity is normalized by $\sigma_{min} = \pi e^2/2h$.

Figure 5.4 and 5.5 show the real and the imaginary parts of n_{eff} versus the thickness of the guiding layer for different values of the film permittivity and permeability, it is clear the product $\varepsilon_2, \mu_2 = 4.0$.

We noted when $\varepsilon_2 = -4$, $\mu_2 = -1$, the effective index n_{eff} has a highest value ($n_{\text{eff}} = 3.7$), when $\varepsilon_2 = -1$, $\mu_2 = -4$, the effective index have a lowest value ($n_{\text{eff}} = 2.35$), when $\varepsilon_2 = \mu_2 = -2$, we have the value ($n_{\text{eff}} = 2.87$).

At the same curve, we plot the RHM at THz region. In Figs. (5.4-5.5), we assumed a RHM film $\varepsilon_2 = 1$, $\mu_2 = 1$.

We noticed that the effective refractive index n_{eff} of RHM film is less than that of a LHM film. This behavior of the n_{eff} can be attributed to following argument. The n_{eff} of a propagating mode is determined by the thickness of the guiding layer and constitutive parameters of the materials constituting the waveguide. For a constant guiding layer thickness it depends solely on the graphene conductivity of the waveguide.

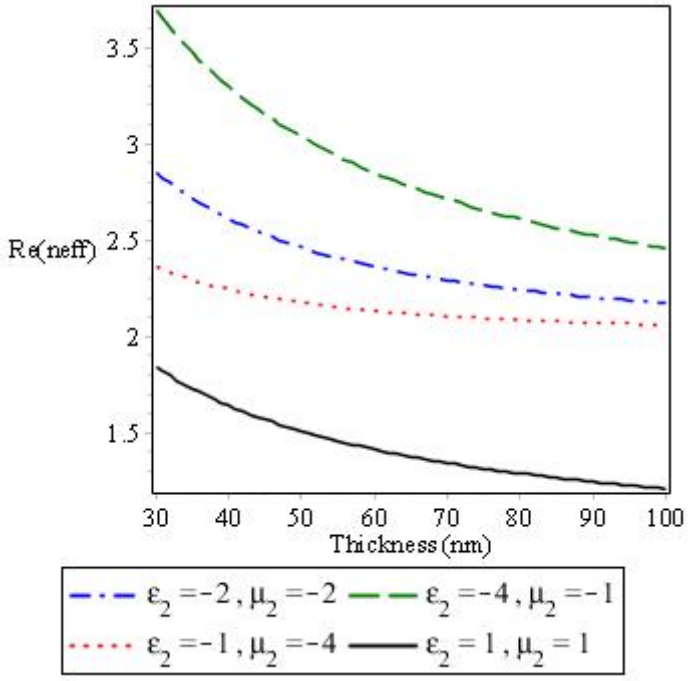

Fig. 5.4 The real part of the effective refractive index (n_{eff}) of the propagating mode versus the thickness of the guiding layer for different values of the core permittivity and permeability for LHM and RHM with d=100nm. The conductivity is normalized by $\sigma = e^2\mu_c\tau/\pi h$, for μ_c = 0.5 eV, and $\tau = 5\times 10^{-13}$.

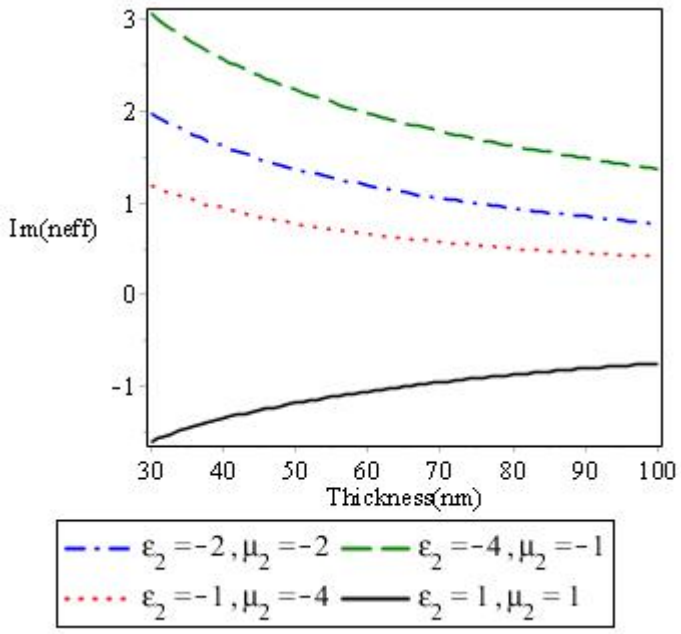

Fig. 5.5 The imaginary part of the effective refractive index (n_{eff}) of the propagating mode versus the thickness of the guiding layer for different values of the core permittivity and permeability for LHM and RHM with d=100nm . The conductivity is normalized by $\sigma = e^2\mu_c\tau/\pi h$, for μ_c = 0.5 eV, and $\tau = 5\times 10^{-13}$.

Fig 5.6 and 5.7 show the real and imaginary parts of the sensitivity of the waveguide sensor as a function of the guiding layer thickness d with four different values of ε_2 and μ_2. The two figures show a positive sensitivity which means that the dependence of the effective refractive index on the upper layer has a positive gradient. The real part of the effective refractive index is much more sensitive to variations of the upper layer than the imaginary part.

It can be seen from Fig. 5.6 that when $\varepsilon_2 = -4$, $\mu_2 = -1$, are optimized for the highest sensitivity. On other hand, for different values of ε_2 and μ_2 at LHM are increasing as the thickness increases.

Moreover, Figs 5.6 and 5.7 show a comparison between the sensitivity of the proposed sensor with the left-handed medium and the sensitivity of right-handed medium. RHM as can be seen in Fig. 5.6, the sensitivity is positive and has a peak at a specific value of the guiding layer thickness *d* (*d* =40nm), then be decaying rapidly when increases of thickness, but at LHM case shows different peaks with the of thickness *d*, and becomes more stability.

In Fig. 5.6 the sensitivity has more stability at different values of ε_2 and μ_2, this due to the presence of the LHM which can significantly increases the sensitivity of sensor.

At imaginary part case which is shown in Fig. 5.7, the values of ε_2 and μ_2 have different peak values. We can see, that when (ε_2 = -2 (-1) and μ_2 = -2 (-4)) the sensitivity started from negative values, then increasing until reaches to positive value, but when ε_2 = -4 and μ_2 = -1 the sensitivity started from positive values then decreasing until reach to negative values. But for right hand case the curve starts from negative then increasing until reaches to positive value.

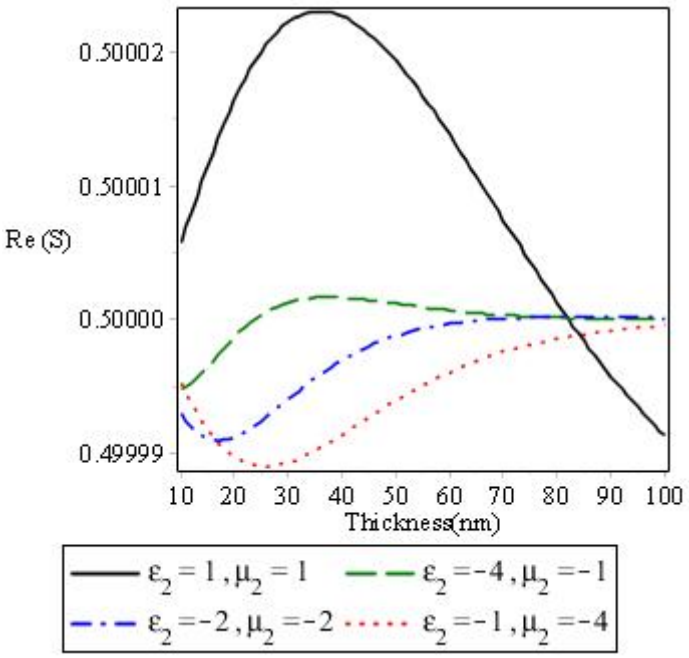

Fig. 5.6 The real part of the sensitivity as a function of the thickness of the LHM layer and RHM layer for different values of ε_2 and μ_2. conductivity is normalized by $\sigma = e^2\mu_c\tau/\pi h$, for f = 500 THz, μ_c = 0.5 eV, and $\tau = 5\times 10^{-13}$.

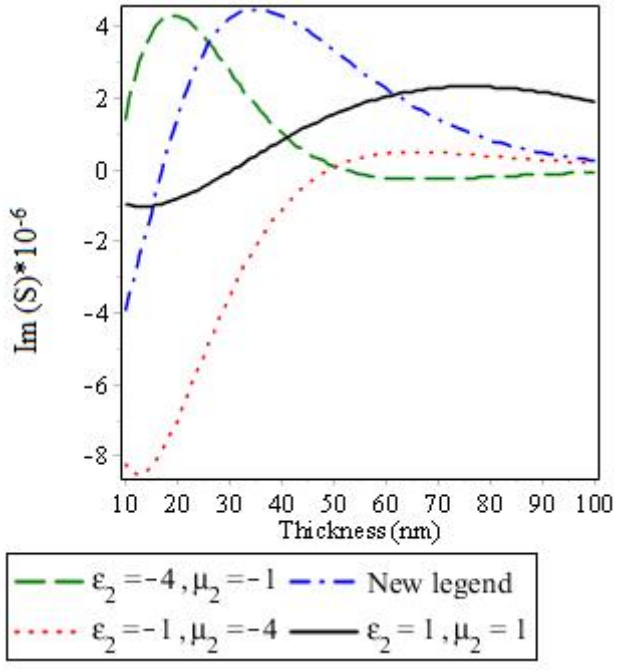

Fig. 5.7 The imaginary part of the sensitivity as a function of the thickness of the LHM layer and RHM layer for different values of ε_2 and μ_2. conductivity is normalized by $\sigma = e^2\mu_c\tau/\pi h$, for f = 500 THz, μ_c = 0.5 eV, and $\tau = 5\times 10^{-13}$.

Fig 5.8 and 5.9 show The real and imaginary parts of the sensitivity of the waveguide sensor as a function of the frequency f with four different values of ε_2 and μ_2. It can be seen from Fig. 5.8 that when ε_2 = -4, μ_2 = -1, are optimized for the highest sensitivity. On other hand, for different values of ε_2 and μ_2 at LHM are increasing with frequency increases.

Moreover, Figs 5.8 and 5.9 show a comparison between the sensitivity of the proposed sensor with the left-handed medium and the sensitivity of right-handed medium. As can be seen in Fig. 5.8, the sensitivity in RHM is positive and has a peak at a specific value of frequency (f =200THz), then be decaying rapidly when increases of frequency f, but at LHM case the sensitivity increases with increasing frequency f, and becomes more stability.

In Fig. 5.8 the sensitivity has more stability at different values of ε_2 and μ_2, this due to the presence of the LHM which can significantly increase the sensitivity of sensor.

Fig 5.9, shows the comparison between the sensitivity of the proposed sensor with the left-handed medium and the sensitivity of right-handed medium at imaginary part. It can be seen that, the sensitivity in RHM is positive and has a peak at a specific value of frequency (f =400THz), then be decaying rapidly when increases of frequency f, also at LHM case the sensitivity decaying rapidly with increasing frequency f.

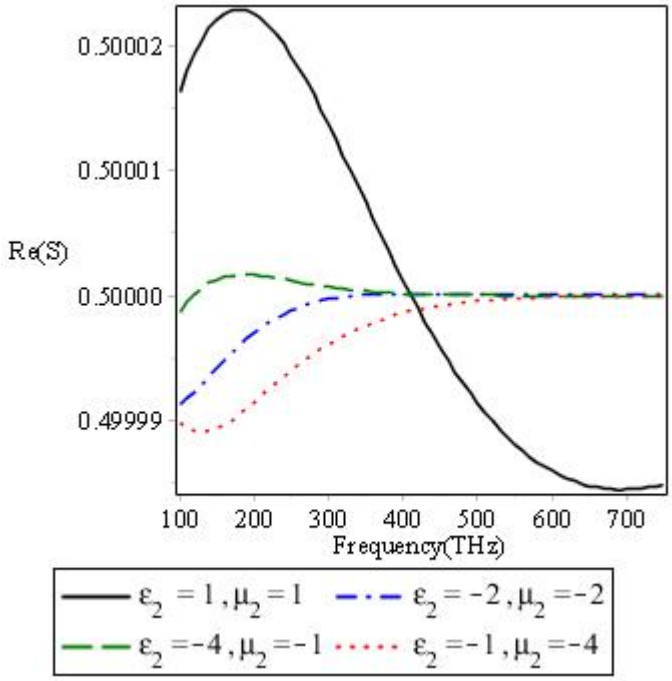

Fig. 5.8 The real part of the sensitivity as a function of the frequency of the LHM layer and RHM layer for different values of ε_2 and μ_2. conductivity is normalized by $\sigma = e^2\mu_c\tau/\pi h$, for d = 100 nm, μ_c = 0.5 eV, and $\tau = 5\times 10^{-13}$.

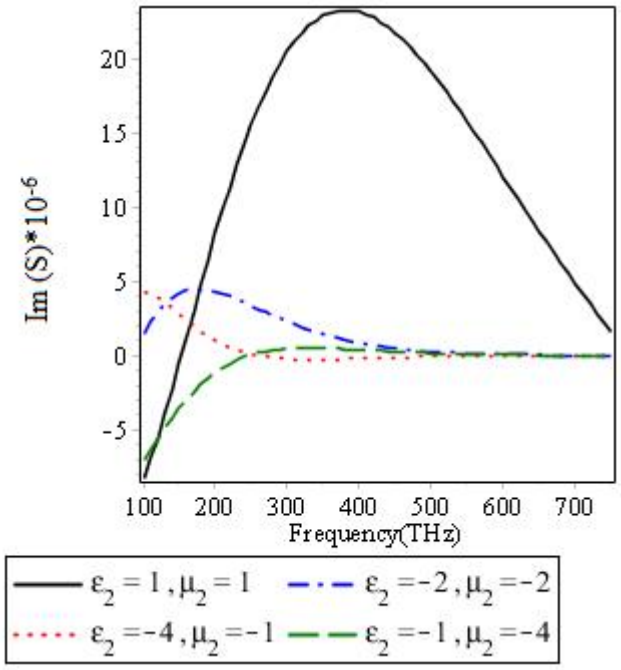

Fig. 5.9 The imaginary part of the sensitivity as a function of the frequency of the LHM layer and RHM layer for different values of ε_2 and μ_2. conductivity is normalized by $\sigma = e^2\mu_c\tau/\pi h$, for d = 100 nm, μ_c = 0.5 eV, and $\tau = 5\times 10^{-13}$.

Chapter Six

Sensitivity at Graphene Left-Hand-Martial Waveguide Structure: (TE Case)

In this chapter, we assume a three-layer planar waveguide consisting of thin left handed material as a guiding layer is investigated for sensing applications. The dispersion relation of TE mode for the proposed waveguide will be derived, the power flowing within each layer will be presented and will be compared to Right-handed material waveguide sensor.

6.1 Structure Analysis

In Fig.5.1 a schematic of the graphene Parallel-plate with LHM is presented. In this section we will discuss the TE (s-polarized) mode.

6.2 The Dispersion Relation of Graphene –LHM (TM-Mode):

The magnetic profiles in the structure region are

$$E_y(x)=\begin{cases} Ae^{-\gamma_1 x}, & x>d/2 \\ B\sin\gamma_2 x+C\cos\gamma_2 x & -d/2\le x\le d/2 \\ De^{\gamma_3 x} & x<-d/2 \end{cases}. \qquad (6.1)$$

The dispersion equation is obtained in similar way as mentioned in the Ch. (5):

$$(c_a+c_b)\cos\gamma_2 d+(1-c_a c_b)\sin\gamma_2 d=0. \qquad (6.2)$$

where

$$c_a = \left(\frac{\mu_2\gamma_1}{\mu_1\gamma_2}\right)\left(1+i\,\frac{\sigma_a\omega\mu_0\mu_1}{\gamma_1}\right)^{-1}, \tag{6.3}$$

$$c_b = \left(\frac{\mu_2\gamma_3}{\mu_3\gamma_2}\right)\left(1+i\,\frac{\sigma_b\omega\mu_0\mu_3}{\gamma_3}\right)^{-1}, \tag{6.4}$$

and $\gamma_j^2 = k_j^2 - \beta^2$.

Taking into account some differences in the new notations k_j ($k_j = \sqrt{\varepsilon_j\mu_j}\,k_0$, $i = 1, 2, 3$), where μ_i have a value (not equal 1).

Eq, (6.2) can be write as:

$$\tan\gamma_2 d = -\frac{(c_a + c_b)}{(1 - c_a c_b)}. \tag{6.5}$$

6.3 Power flowing within the PPWG graphene (TE mode)

The power flow in the structure is:

$$P_{total} = \frac{\beta}{2\omega}\int_{-\infty}^{\infty}\frac{\left|H_y(x)\right|^2}{\varepsilon(x)}dx; \tag{6.6}$$

$$P_{TEtotal} = P_1 + P_2 + P_3. \tag{6.7}$$

Substituting for $H_y(x)$ form Eq. (6.1) into Eq. (6.6), we get:

$$P_1 = -\frac{\beta A^2}{4\omega\mu_0\mu_1\gamma_1} e^{\gamma_1 d} \tag{6.8a}$$

$$P_2 = \frac{\beta}{4\omega\mu_0\mu_2}\left[\left(B^2 + C^2\right)d - \left(B^2 - C^2\right)\cdot\frac{\sin(\gamma_2 d)}{\gamma_2}\right] \tag{6.8b}$$

$$P_3 = -\frac{\beta D^2}{4\omega\mu_0\mu_3\gamma_3} e^{-\gamma_3 d} \tag{6.8c}$$

Then

$$P_{TMtotal} = -\frac{\beta}{4\omega\mu_0}\left\{\left(\frac{A^2 e^{\gamma_1 d}}{\mu_1\gamma_1} + \frac{D^2 e^{\gamma_3 d}}{\mu_3\gamma_3}\right) - \frac{\left(B^2 + C^2\right)}{\mu_2} d + \left(B^2 - C^2\right)\cdot\frac{\sin(\gamma_2 d)}{\mu_2\gamma_2}\right\}. \tag{6.9}$$

The coefficients *A, B, C* and *D* are related to each other through the equations:

$$B = A\left\{\sin(\gamma_2 d/2) - \left(\frac{\gamma_1\mu_2}{\gamma_2\mu_1}\right)\left(1 + i\,\frac{\sigma_a\omega\mu_1\mu_0}{\gamma_1}\right)\cdot\cos(\gamma_2 d/2)\right\}\cdot e^{-\gamma_1 d/2}, \tag{6.10}$$

$$C = A\left\{\cos(\gamma_2 d/2) + \left(\frac{\gamma_1\mu_2}{\gamma_2\mu_1}\right)\left(1 + i\,\frac{\sigma_a\omega\mu_1\mu_0}{\gamma_1}\right)\cdot\sin(\gamma_2 d/2)\right\}\cdot e^{-\gamma_1 d/2}, \tag{6.11}$$

$$D = \frac{A\left\{\sin(\gamma_2 d/2) - \left(\frac{\gamma_1\mu_2}{\gamma_2\mu_1}\right)\left(1 + i\,\frac{\sigma_a\omega\mu_1\mu_0}{\gamma_1}\right)\cdot\cos(\gamma_2 d/2)\right\}\cdot e^{-\gamma_1 d/2}}{\left\{-\sin(\gamma_2 d/2) + \left(\frac{\gamma_3\mu_2}{\gamma_2\mu_3}\right)\left(1 + i\,\frac{\sigma_b\omega\mu_3\mu_0}{\gamma_3}\right)\cdot\cos(\gamma_2 d/2)\right\}\cdot e^{-\gamma_3 d/2}}, \tag{6.12}$$

The Sensitivity is given by:

$$S = \frac{P_1}{P_{total}}, \tag{6.13}$$

$$== \frac{A^2 e^{\gamma_1 d}}{\mu_1\gamma_1\left\{\left(\frac{A^2 e^{\gamma_1 d}}{\mu_1\gamma_1} + \frac{D^2 e^{\gamma_3 d}}{\mu_3\gamma_3}\right) - \frac{(B^2 + C^2)d}{\mu_2} + (B^2 - C^2)d\cdot\frac{\sin(\gamma_2 d)}{\mu_2\gamma_2}\right\}}. \tag{6.14}$$

6.4 Numerical results

We have considered two laterally infinite graphene sheets spaced a distance d apart with $\varepsilon_1 = \varepsilon_3 = 1$ and $\mu_1 = \mu_3 = 1$. The LHM layer is sandwiched between a graphene sheet .

Fig 6.1 and 6.2 show the real and the imaginary parts of the of n_{eff} from eq. (6.5) of LHM layer with plate separation d=100 μm, for frequencies in the THz frequency for different values of ε_2 and μ_2 .

We noted that when $\varepsilon_2 = -4$, $\mu_2 = -1$, the effective index has a highest value ($n_{\text{eff}} = 0.9$), when $\varepsilon_2 = -1$, $\mu_2 = -4$, the effective index has a lowest value ($n_{\text{eff}} = 0.4$), when $\varepsilon_2 = \mu_2 = -2$, we have the value ($n_{\text{eff}} = 0.4$).

Additionally, when frequency is increasing, the three curves converge at specific value ($n_{\text{eff}} = 1.4$).

Moreover, the effective index n_{eff} increases as the frequency increases as shown in Fig. 6.1, for LHM, but for RHM the real part is decreasing.

Fig 6.2 shows the imaginary part of the n_{eff} decreases with increasing frequency, but for RHM is increasing.

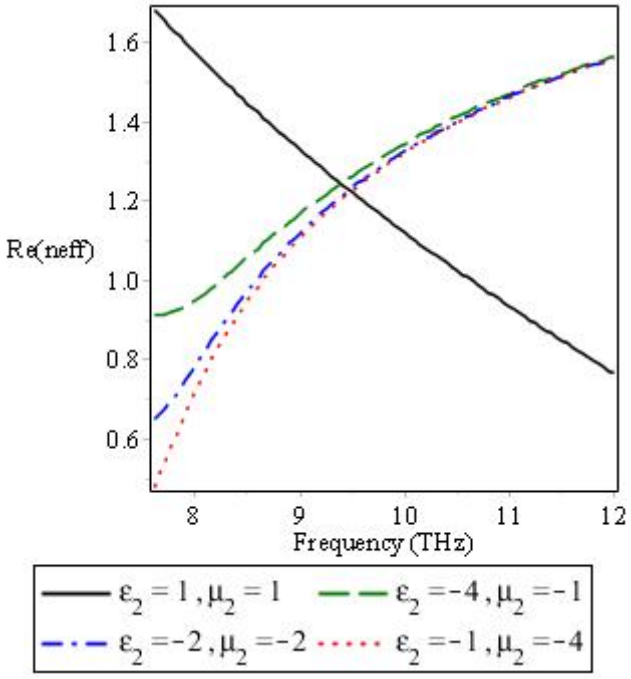

Fig. 6.1. The real part of the effective index n_{eff} from Eq. (6.5) versus the frequency of the guiding layer for different values of the core permittivity and permeability for LHM and RHM with d=100μm. The conductivity is normalized by $\sigma = e^2\mu_c\tau/\pi h$, for μ_c = 0.5 eV, and $\tau = 5\times 10^{-13}$.

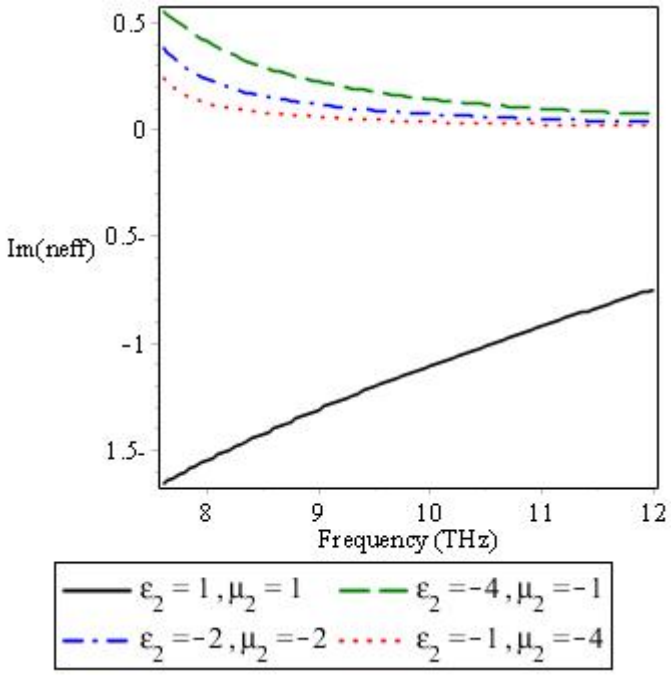

Fig. 6.2. The imaginary part of n_{eff} from Eq. (6.5) versus the frequency of the guiding layer for different values of the core permittivity and permeability for LHM and RHM with d=100μm . The conductivity is normalized by $\sigma = e^2\mu_c\tau/\pi h$, for μ_c = 0.5 eV, and $\tau = 5\times 10^{-13}$.

Fig 6.3 and 6.4 show that, the real and the imaginary parts of the effective index n_{eff} from eq. (6.5) of LHM layer with plate separation f =8.5 THz.

In Fig 6.3 we noted when ε_2 = -4 , μ_2= -1, the effective index have a highest value (n_{eff} = 1.57), when ε_2 = -1 , μ_2= -4, the effective index have a lowest value (n_{eff} = 0.968), when $\varepsilon_2 = \mu_2$= -2, we have the a value (n_{eff} = 0.941).

Additionally, when thickness increasing the three curves converge at specific value (n_{eff} =1.4). At the same curve, we graph the RHM at THz region, where assumed a RHM layer ε_2 = 1 , μ_2= 1.

Fig 6.4 shows the imaginary part of the effective index n_{eff} decreases with increasing frequency, but for RHM is increasing.

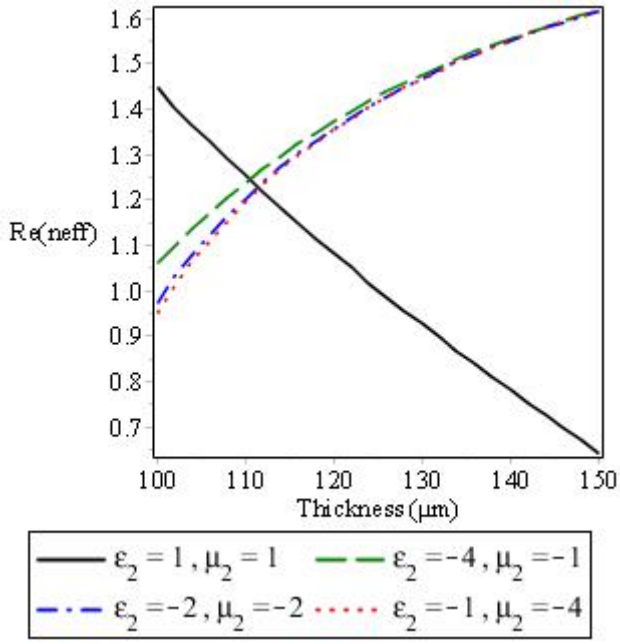

Fig. 6.3. The real part of the effective index n_{eff} from Eq. (6.5) versus the thickness of the guiding layer for different values of the core permittivity and permeability for LHM and RHM with f =8.5 THz . The conductivity is normalized by $\sigma = e^2\mu_c\tau/\pi h$, for μ_c = 0.5 eV, and $\tau = 5\times 10^{-13}$.

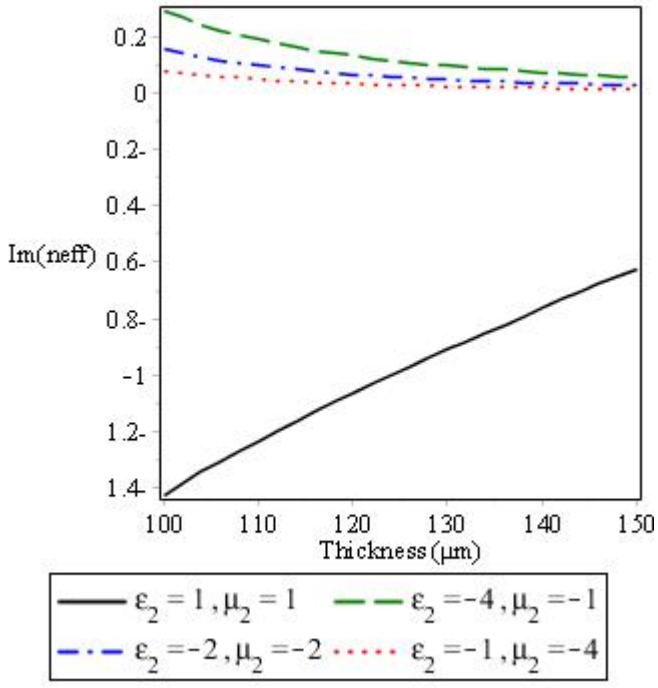

Fig. 6.4. The imaginary part of the effective index n_{eff} from Eq. (6.5) versus the thickness of the guiding layer for different values of the core permittivity and permeability for LHM and RHM with f =8.5 THz . The conductivity is normalized by $\sigma = e^2\mu_c\tau/\pi h$, for μ_c = 0.5 eV, and $\tau = 5\times 10^{-13}$.

Fig 6.5 and 6.6 show the real and imaginary parts of the sensitivity of the waveguide sensor as a function of the guiding layer thickness d with four different values of ε_2 and μ_2. The two figures show a positive sensitivity. The real part of the effective refractive index is much more sensitive to variations of the upper layer than the imaginary part.

It can be seen from Fig. 6.5 that when ε_2 = -1, μ_2 = -4, are optimized for the highest sensitivity. On other hand, for different values of ε_2 and μ_2 at LHM are increasing with the film thickness increasing. Moreover, Figs 6.5 and 6.6 show a comparison between the sensitivity of the proposed sensor with the left-handed medium and the sensitivity of right-handed medium.

As can be seen in Fig. 6.5, the sensitivity in RHM is positive and has a peak at a specific value of the guiding layer thickness d (d =170μm), then be decaying rapidly when increases of thickness, but at LHM case the sensitivity increases with increasing the guiding layer thickness d, and becomes more stable for RHM. We found the sensitivity has more stability at different values of ε_2 and μ_2, this due to the presence of the LHM, can significantly increases the sensitivity of sensor.

At imaginary part case which is shown in Fig. 6.6, the values of ε_2 and μ_2 have a differed behaviour. We can see that, when (ε_2 = -2 (-4) and μ_2 = -2 (-1)) the sensitivity deceasing, but when ε_2 = -1 and μ_2 = -4 the sensitivity is increasing. Moreover, we are comparing between the sensitivity of the proposed sensor with the left-handed medium and the sensitivity of right-handed medium. It can be seen, the sensitivity in RHM is negative and has a peak at a specific value of the guiding layer thickness d (d=170μm), then decaying rapidly when the thickness are increased, also at LHM case the sensitivity is decreasing with increasing thickness d.

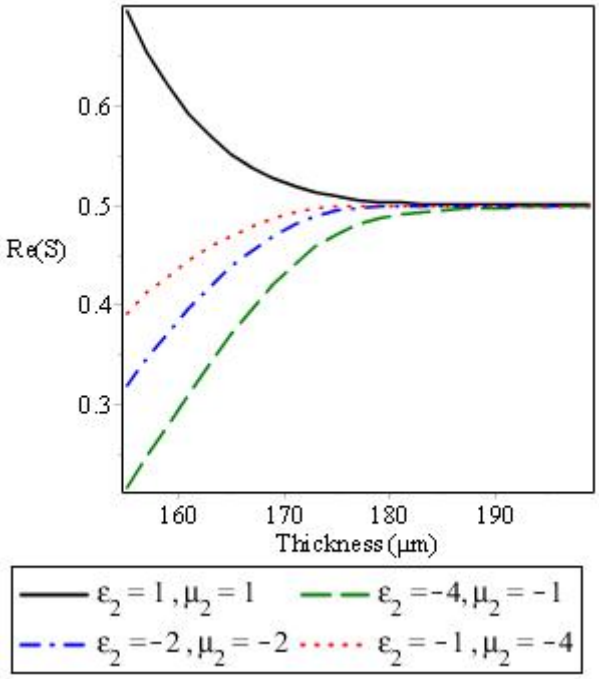

Fig. 6.5 The real part of the sensitivity as a function of the thickness of the LHM layer and RHM layer for different values of ε_2 and μ_2. Conductivity is normalized by $\sigma = e^2\mu_c\tau/\pi h$, for f = 8.5 THz, μ_c = 0.5 eV, and $\tau = 5\times 10^{-13}$.

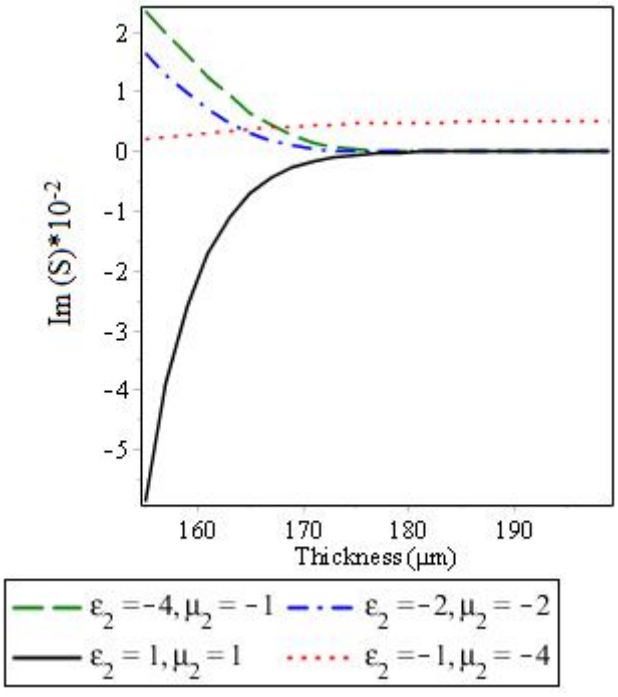

Fig. 6.6 The imaginary part of the sensitivity as a function of the thickness of the LHM layer and RHM layer for different values of ε_2 and μ_2. conductivity is normalized by $\sigma = e^2\mu_c\tau/\pi h$, for f = 8.5 THz, μ_c = 0.5 eV, and $\tau = 5\times 10^{-13}$.

Fig 6.7 and 6.8 show The real and imaginary parts of the sensitivity of the waveguide sensor as a function of the frequency *f* with four different values of ε_2 and μ_2.

It can be seen from fig. 6.7 that when ε_2 = -1, μ_2 = -4, are optimized for the highest sensitivity. On other hand, for different values of ε_2 and μ_2 of LHM the sensitivity is increasing with the frequency increases.

Moreover, figs 6.7 and 6.8 show a comparison between the sensitivity of the proposed sensor with the left-handed medium and the sensitivity of right-handed medium. As shown in Fig. 6.7, the sensitivity in RHM is positive and has a peak at a specific value of frequency (*f* =10THz), then decaying rapidly when increases of frequency *f*, but at LHM case the sensitivity increases with increasing the frequency *f*, and becomes more stable. The sensitivity has more stability at different values of ε_2 and μ_2, this due to the presence of the LHM, which can significantly increases the sensitivity of sensor.

In fig 6.8, show the comparison between the sensitivity of the proposed sensor with the left-handed medium and the sensitivity of right-handed medium at imaginary part. It can be seen, the sensitivity in RHM is negative and has a peak at a specific value of frequency (*f* =10THz), then be decaying rapidly when increases of frequency *f*, also at LHM case the sensitivity decreasing as increasing of the frequency *f*.

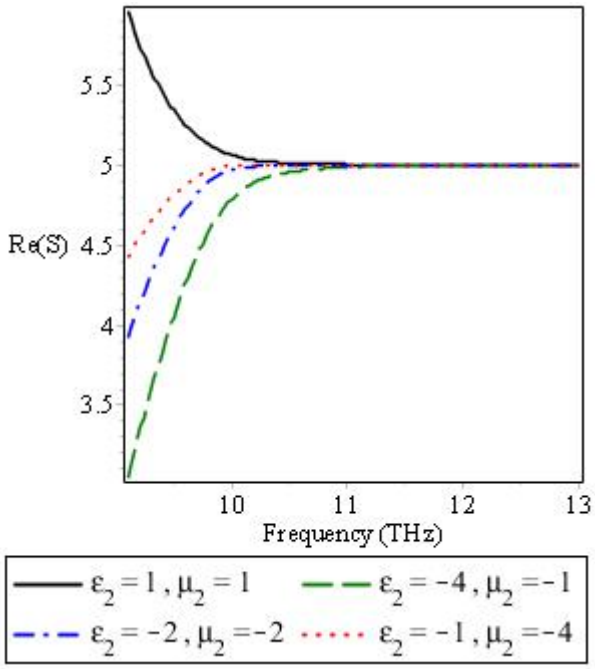

Fig. 6.7 The real part of the sensitivity as a function of the frequency of the LHM layer and RHM layer for different values of ε2 and μ2. conductivity is normalized by $\sigma = e2\mu_c\tau/\pi h$, for d = 150 μm, μ_c = 0.5 eV, and $\tau = 5\times 10^{-13}$.

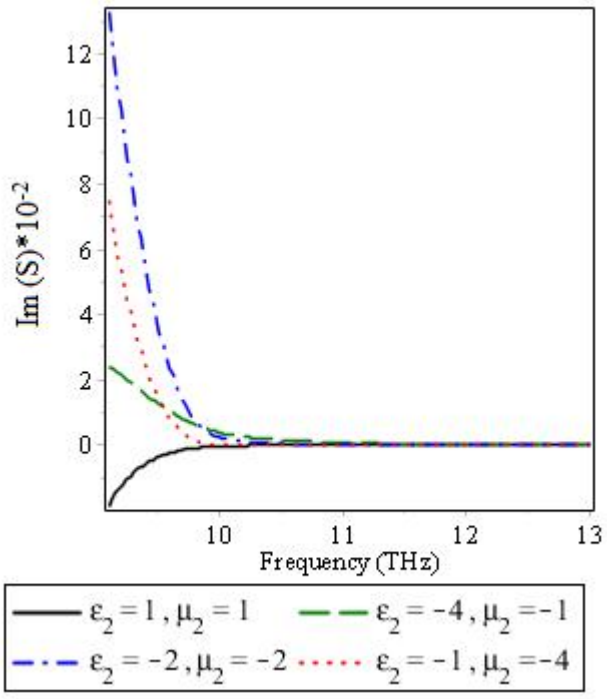

Fig. 6.8 The imaginary part of the sensitivity as a function of the frequency of the LHM layer and RHM layer for different values of ε2 and μ2. conductivity is normalized by $\sigma = e2\mu_c\tau/\pi h$, for *d* = 150 μm, μ_c = 0.5 eV, and $\tau = 5\times 10^{-13}$.

Results :

1- Dispersion relation:

- We have demonstrated that TE and TM modes existing in the Gega/Terahertz frequency ranges.
- The characteristics of guided modes in waveguide structure with two graphene layers have been compared to those of modes in dielectric Left-handed materials nanostructures/microstructures.
- We note that the TE mode has almost linear dispersion and small losses. This is a consequence of the small degree of localization of this mode and indicates that it is nearly equivalent to a plane wave propagating in free space.
- In contrast, TM polarized modes are strongly localized as a consequence, which are characterized by small propagation lengths and strong dispersion. This differs markedly from that of a plane electromagnetic wave in free space.

2- Sensitivity

At PPWG- dielectric (TM- Case):

- The real part of the sensitivity of the proposed sensor versus the thickness of the dielectric layer for different values of the frequencies is positive and increasing with increasing the thickness and the value of frequency.
- The imaginary part of the sensitivity of the proposed sensor versus the thickness of the dielectric layer for different values of the frequencies is negative.

- The Re(S) and Im(S) of the proposed sensor versus the frequencies of the dielectric layer for different values of the Thickness are positive and increases with increasing frequency and values of thickness.

At PPWG- dielectric (TE- Case):

- The real part of the sensitivity of the proposed sensor versus the thickness for different values of the frequencies is positive and decreases with increasing thickness. Also the sensitivity decreases with increasing the value of frequency.
- The imaginary part of the sensitivity of the proposed sensor versus the thickness of the dielectric layer for different values of the frequencies is negative.
- The real part of the sensitivity of the proposed sensor versus the frequencies of the dielectric layer for different values of the thickness exhibit different behaviors with *d*.
- The Re(S) at (d = 150 μm) is positive and has a peak at specific value of the frequency then decreasing with increasing frequency.
- The imaginary part of the sensitivity of the proposed sensor versus the frequencies of the dielectric layer for different values of the thickness exhibit different behaviors with *d*.
- The Im(S) at (d = 150 μm) is positive and has a peak at specific value of the frequency then decreasing with decreasing the operating frequency.

At PPWG- LHM (TM- Case):

- The real part of the sensitivity versus the thickness of the LHM layer and RHM layer for different values of ε_2 and μ_2 are positive.
- The imaginary part of the sensitivity versus the thickness of the LHM layer for different values of ε_2 and μ_2 exhibit different behaviors with d.
- The real part of the sensitivity versus the frequency of the LHM layer and RHM layer for different values of ε_2 and μ_2 are positive.
- The imaginary part of the sensitivity versus the frequency of the LHM layer and RHM layer for different values of ε_2 and μ_2 exhibit different behaviors with f.

At PPWG- LHM (TE- Case):

- The real part of the sensitivity versus the thickness of the LHM layer for different values of ε_2 and μ_2 are positive.
- The imaginary part of the sensitivity versus the thickness of the LHM layer and RHM layer for different values of ε_2 and μ_2 exhibit different behaviors with d.
- The real part of the sensitivity versus the frequency of the LHM layer for different values of ε_2 and μ_2 are positive.
- The imaginary part of the sensitivity versus the frequency of the LHM layer and RHM layer for different values of ε_2 and μ_2 exhibit different behaviors with f. The LHM is positive but RHM is negative

Conclusion

- Our study of guided waves in graphene-based structures will allow the better understanding of how to incorporate them in electromagnetic devices.
- The comparing between the structure with dielectric layer and structure contain Left-hand-material will be presented. Also, the sensitivity of the sensor to changes of the permittivity and magnetic permeability for LHM will be presented.
- Our results are important for a better understanding of Graphene Parallel Plate Waveguide with Left-handed Material which are useful to design the various graphene-bases optoelectronic devices.

References:

1. Geim, A.K. and Novoselov, K.S. *The Rise of Graphene.* Nature materials, 2007. **6**(3): p. 183-191.
2. Dresselhaus, M.S., Dresselhaus, G., and Eklund, P.C. *Science of Fullerenes and Carbon Nanotubes: Their Properties And Applications*. 1996: Academic press.
3. Chen, H., et al. *Mechanically Strong, Electrically Conductive, And Biocompatible Graphene Paper.* Advanced Materials, 2008. **20**(18): p. 3557-3561.
4. Armand, M., and Tarascon, J.-M. *Building Better Batteries.* Nature, 2008. **451**(7179): p. 652-657.
5. Gasnier, A., Pedano, Mlaura R., Maria D., and Gustavo, A. *Graphene Paste Electrode: Electrochemical Behavior And Analytical Applications For The Quantification of NADH.* Sensors and Actuators B: Chemical, 2013. **176**: p. 921-926.
6. Zou, Y., Tassin P., Koschny T., and Soukoulis M. *Interaction Between Graphene And Metamaterials: split rings vs. wire pairs.* Optics express, 2012. **20**(11): p. 12198-12204.
7. Fal'Ko, V., and Geim, A. *Graphene: Emerging Matter In Two Dimensions.* The European Physical Journal-Special Topics, 2007. **148**(1): p. 1-4.
8. Geim, A.K. *Graphene: status and prospects.* Science, 2009. **324**(5934): p. 1530-1534.
9. Nagayoshi, H., Nakao, K., and Uemura, Y. *Band Theory of Graphite. I. Formalism of a New method of Calculation and the Fermi Surface of Graphite.* Journal of the Physical Society of Japan, 1976. **41**(5): p. 1480-1487.
10. Wallace, P.R. *The Band Theory Of Graphite.* Physical Review, 1947. **71**(9): p. 622.
11. McClure, J. *Theory Of Diamagnetism Of Graphite.* Physical Review, 1960. **119**(2): p. 606.
12. Curl, R.F. *Dawn Of The Fullerenes: Experiment And Conjecture.* Reviews Of Modern Physics, 1997. **69**(3): p. 691-702.
13. Harris, P.J., and Harris, P.J.F. *Carbon Nanotubes And Related Structures: New Materials For The Twenty-First Century*. 2001: Cambridge university press.
14. Novoselov, K., Morozov, S., Mohinddin, T., Ponomarenko, L., Elias, D., Yang, R., Barbolina, I. Blake, P., Booth, T., Jiang, D. Electronic Properties Of Graphene. Physica Status Solidi (b), 2007. 244(11): p. 4106-4111.
15. Katsnelson, M.I., *Graphene: Carbon In Two Dimensions.* Materials Today, 2007. **10**(1): p. 20-27.

16. Oshima, C. and Nagashima, A. *Ultra-Thin Epitaxial Films Of Graphite And Hexagonal Boron Nitride On Solid Surfaces.* Journal of Physics: Condensed Matter, 1997. **9**(1): p. 1.
17. Meyer, J.C., Geim, A. K., Katsnelson, M., Novoselov, K., Booth, T., Roth, S. *The Structure Of Suspended Graphene Sheets.* Nature, 2007. **446**(7131): p. 60-63.
18. Neto, A.C., Guinea, F., Peres, N., Novoselov, K. S., Geim, A. K. *The Electronic Properties Of Graphene.* Reviews Of Modern Physics, 2009. **81**(1): p. 109.
19. Dragoman, M., Neculoiu, D., Dragoman, D., Deligeorgis, G., Konstantinidis, G., Cismaru, A., Coccetti, F., Plana, R. *Graphene For Microwaves.* Microwave Magazine, IEEE, 2010. **11**(7): p. 81-86.
20. Yu, X. *FDTD Modeling of Graphene-Based RF Devices: Fundamental Aspects and Applications*. 2013, University of Toronto.
21. Moon, J.-S., and Gaskill, D.K. *Graphene: Its fundamentals to future applications.* Microwave Theory and Techniques, IEEE Transactions on, 2011. **59**(10): p. 2702-2708.
22. Gusynin, V., Sharapov, S., and Carbotte, J. *Magneto-optical conductivity in graphene.* Journal of Physics: Condensed Matter, 2007. **19**(2): p. 026222.
23. Hanson, G.W. *Dyadic Green's Functions And Guided Surface Waves For A Surface Conductivity Model Of Graphene.* Journal of Applied Physics, 2008. **103**(6): p. 064302.
24. Falkovsky, L. *Optical Properties Of Graphene*. In *Journal Of Physics: Conference Series*. 2008: IOP Publishing.
25. Gusynin, V., Sharapov, S., and Carbotte, J. *Unusual Microwave Response Of Dirac Quasiparticles In Graphene.* Physical review letters, 2006. **96**(25): p. 256802.
26. Ziegler, K. *Minimal Conductivity Of Graphene: Nonuniversal Values From The Kubo Formula.* Physical Review B, 2007. **75**(23): p. 233407.
27. Brownson, D.A., Kampouris, D.K., and Banks, C.E. *An Overview Of Graphene In Energy Production And Storage Applications.* Journal of Power Sources, 2011. **196**(11): p. 4873-4885.
28. Kötz, R., and Carlen, M. *Principles And Applications Of Electrochemical Capacitors.* Electrochimica Acta, 2000. **45**(15): p. 2483-2498.
29. Snook, G.A., Kao, P., and Best, A.S. *Conducting-Polymer-Based Supercapacitor Devices And Electrodes.* Journal of Power Sources, 2011. **196**(1): p. 1-12.
30. Ramachandran, R., Mani, Veerappan C., Shen-Ming, S., Ramiah, L., and Bih-Show. *Recent Trends in Graphene based Electrode Materials for Energy Storage Devices and Sensors Applications.* International Journal of Electrochemical Science, 2013. **8**(10).

31. Zhou, G., Wang, D., Li, F., Zhang, L., Li, N., Wu, Z., Wen, L., Lu, G., and Cheng, H. *Graphene-wrapped Fe3O4 anode material with improved reversible capacity and cyclic stability for lithium ion batteries.* Chemistry of Materials, 2010. **22**(18): p. 5306-5313.
32. Chen, S., Gordin, M. L., Yi, R., Howlett, G., Sohn, H., and Wang, D. *Silicon Core–Hollow Carbon Shell Nanocomposites With Tunable Buffer Voids For High Capacity Anodes Of Lithium-Ion Batteries.* Physical Chemistry Chemical Physics, 2012. **14**(37): p. 12741-12745.
33. Wang, C., Waje, M., Wang, X., Tang, J. M., Haddon, R. C., and Yan, Y. *Proton exchange membrane fuel cells with carbon nanotube based electrodes.* Nano letters, 2004. **4**(2): p. 345-348.
34. Kim, D., Lee, J., Lee, G., Overzet, L., Kozlov, M., Aliev, A., Park, Y., and Yang, D. *Carbon nanotubes based methanol sensor for fuel cells application.* Journal of nanoscience and nanotechnology, 2006. **6**(11): p. 3608-3613.
35. Kim, H., Choi, H., Hwang, S., Kim, Y., and Jeon, M. *Fabrication and characterization of carbon-based counter electrodes prepared by electrophoretic deposition for dye-sensitized solar cells.* Nanoscale research letters, 2012. **7**(1): p. 1-4.
36. Chen, X., Zhu, J., Xi, Q., and Yang, W. *A High Performance Electrochemical Sensor For Acetaminophen Based On Single-Walled Carbon Nanotube–Graphene Nanosheet Hybrid Films.* Sensors and Actuators B: Chemical, 2012. **161**(1): p. 648-654.
37. Nasri, Z., and Shams, E. *A Glucose Biosensor Based On Direct Electron Transfer Of Glucose Oxidase Immobilized Onto Glassy Carbon Electrode Modified With Nitrophenyl Diazonium Salt.* Electrochimica Acta, 2013. **112**: p. 640-647.
38. Wang, Y., Joshi, P.P., Hobbs, K.L., Johnson, M.B., and Schmidtke, D.W. *Nanostructured Biosensors Built By Layer-By-Layer Electrostatic Assembly Of Enzyme-Coated Single-Walled Carbon Nanotubes And Redox Polymers.* Langmuir, 2006. **22**(23): p. 9776-9783.
39. Lu, G., L.E. Ocola, and Chen, J. *Gas Detection Using Low-Temperature Reduced Graphene Oxide Sheets.* Applied Physics Letters, 2009. **94**(8): p. 083111.
40. Gong, J., Guan, Z., and Song, D. *Biosensor Based On Acetylcholinesterase Immobilized Onto Layered Double Hydroxides For Flow Injection/Amperometric Detection Of Organophosphate Pesticides.* Biosensors and Bioelectronics, 2013. **39**(1): p. 320-323.
41. Cesarino, I., Moraes, F.C., Lanza, M.R., and Machado, S.A. *Electrochemical Detection Of Carbamate Pesticides In Fruit And Vegetables With A Biosensor Based On Acetylcholinesterase Immobilised On A Composite Of Polyaniline–Carbon Nanotubes.* Food Chemistry, 2012. **135**(3): p. 873-879.

42. Wu, S., Lan, X., Cui, L., Zhang, L., Tao, S., Wang, H., Han, M., Liu, Z., and Meng, C. *Application Of Graphene For Preconcentration And Highly Sensitive Stripping Voltammetric Analysis Of Organophosphate Pesticide.* Analytica chimica acta, 2011. **699**(2): p. 170-176.
43. Pacheco, J. *Theory And Application Of Left-Handed Metamaterials*. 2004, Massachusetts Institute Of Technology.
44. Liu, Y., and Zhang, X. *Metamaterials: A New Frontier Of Science And Technology.* Chemical Society Reviews, 2011. **40**(5): p. 2494-2507.
45. Caloz, C., and Itoh, T. *Electromagnetic Metamaterials: Transmission Line Theory And Microwave Applications*. 2005: John Wiley & Sons.
46. Veselago, V.G. *The Electrodynamics Of Substances With Simultaneously Negative index values of ε and μ.* Physics-Uspekhi, 1968. **10**(4): P. 509-514.
47. Cai, W., and Shalaev, V.M. *Optical Metamaterials*. Vol. 10. 2010: Springer.
48. Rahim, A., and Kamal, M. *Process For Constructing The Metamaterials And Studying Its Advancement In Microwave Circuits.* 2008.
49. Ramakrishna, S.A., and Grzegorczyk, T.M. *Negative Refractive Index Materials*. 2009, SPIE Press, Washington.
50. Fu, C., Tanner, D., and Zhang, Z. *Energy Transmission By Photon Tunneling In Multilayer Structures Including Negative Index Materials.* Journal of heat transfer, 2005. **127**(9): p. 1046-1052.
51. Reza, A. *The Optical Properties Of Metamaterial Waveguide Structures.* Master thesis, Queens Univesity, Canda, 2008.
52. El-Amassi, D.M., and Shabat, M.M. *Left–Handed Photonic Crystal Sensor, Analytical Approach. Master Thesis, Islmaic Univesity, 2013.*
53. Pendry, J.B., Holden, A.J., Robbins, D., and Stewart, W. *Magnetism From Conductors And Enhanced Nonlinear Phenomena.* Microwave Theory and Techniques, IEEE Transactions on, 1999. **47**(11): p. 2075-2084.
54. Smith, D.R., Padilla, W.J., Vier, D.C., Nemat-Nasser, S.C., and Schultz, S. *Composite Medium With Simultaneously Negative Permeability And Permittivity.* Physical Review Letters, 2000. **84**(18): p. 4184.
55. Kong, J. *Electromagnetic Wave Interaction With Stratified Negative Isotropic Media.* Progress In Electromagnetics Research, 2002. **35**: p. 1-52.
56. Engheta, N. *Metamaterials With Negative Permittivity And Permeability: Background, Salient Features, And New Trends.* Departmental Papers (ESE), 2003: p. 9.
57. Chew, W.C. *Some Reflections On Double Negative Materials.* Progress In Electromagnetics Research, 2005. **51**: p. 1-26.
58. Sabah, C., and Uckun, S. *Electromagnetic Wave Propagation Through Frequency-Dispersive And Lossy Double-Negative Slab.* Opto-Electronics Review, 2007. **15**(3): p. 133-143.

59. Schurig, D., Mock, J.J., Justice, B.J., Cummer, S.A., Pendry, J.B., Starr, A.F., and Smith, D.R. *Metamaterial Electromagnetic Cloak At Microwave Frequencies.* Science, 2006. **314**(5801): p. 977-980.
60. Grbic, A., and Eleftheriades, G.V. *Overcoming The Diffraction Limit With A Planar Left-Handed Transmission-Line Lens.* Physical Review Letters, 2004. **92**(11): p. 117403.
61. Niu, W., Huang, M., Xiao, Z., and Yang, J. *Sensitivity Enhancement In Optical Waveguide Sensors Based On TM Wave And Metamaterials*. In *Antennas Propagation and EM Theory (ISAPE), 2010 9th International Symposium on*. 2010: IEEE.
62. El-Khozondar, H., Shabat, M.M., El-Khozondar, R.J., and Koch, A.W. *Stress effect on optical nonlinear waveguide sensor.* Journal of Optical Communications, 2007. **28**(3): p. 175-179.
63. Parriaux, O., and Veldhuis, G. *Normalized Analysis For The Sensitivity Optimization Of Integrated Optical Evanescent-Wave Sensors.* Journal of lightwave technology, 1998. **16**(4): p. 573.
64. Verma, A., Prajapati, Y., Ayub, S., Saini, J.P., and Singh, V. *Analytical Analysis Of Sensitivity Of Optical Waveguide Sensor.* International Journal of Engineering, Science and Technology, 2011. **3**(3).
65. Harris, R., and Wilkinson, J.S. *Waveguide surface plasmon resonance sensors.* Sensors and Actuators B: Chemical, 1995. **29**(1): p. 261-267.
66. Taya, S.A., Shabat M.M., and Khalil H.M. *Nonlinear Planar Asymmetrical Optical Waveguides For Sensing Applications.* Optik-International Journal for Light and Electron Optics, 2010. **121**(9): p. 860-865.
67. Shabat M.M., Taya, S.A., Khalil, H.M., and vJäger, D.S. *Theoretical Analysis Of TM Nonlinear Asymmetrical Waveguide Optical Sensors.* Sensors and Actuators A: Physical, 2008. **147**(1): p. 137-141.
68. Shabat, M.M., Taya, S.A., Khalil, H.M., and Abadla, M.M. *Analysis of the sensitivity of self-focused nonlinear optical evanescent waveguide sensors.* International Journal of Optomechatronics, 2007. **1**(3): p. 284-296.
69. Taya, S.A., Shabat, M.M., El-Agez, T.M., Kullab, H.M., and Abadla, M.M. *Theoretical study of slab waveguide optical sensor with left-handed material as a core layer.* Optica applicata, 2012. **42**(1): p. 193-205.
70. Khalil, H.M., Shabat, M.M., Taya, S.A., and Abadla, M.M. *Nonlinear optical waveguide structure for sensor application: TM case.* International Journal of Modern Physics B, 2007. **21**(30): p. 5075-5089.
71. Taya, S.A., Shabat, M.M., and Khalil, H. *Enhancement Of Sensitivity In Optical Waveguide Sensors Using Left-Handed Materials.* Optik-International Journal for Light and Electron Optics, 2009. **120**(10): p. 504-508.

72. Horvath, R., Pedersen, H.C., and Larsen, N.B. *Demonstration Of Reverse Symmetry Waveguide Sensing In Aqueous Solutions.* Applied physics letters, 2002. **81**(12): p. 2166-2168.
73. Veldhuis, G.J. *Bent-Waveguide Devices and Mechano-Optical Switches*. 1998: Universiteit Twente.
74. Horváth, R., Pedersen, H.C., Skivesen, N., Selmeczi, D., and Larsen, N.B. *Optical Waveguide Sensor For On-Line Monitoring Of Bacteria.* Optics letters, 2003. **28**(14): p. 1233-1235.
75. Monk, P. *Finite Element Methods For Maxwell's Equations*. 2003: Oxford University Press.
76. Kawano, K., and Kitoh, T. *Frontmatter and Index*. 2001: Wiley Online Library.
77. Kawano, K., and Kitoh, T. *Introduction to Optical Waveguide Analysis: Solving Maxwell's Equation and the Schrödinger Equation*. 2004: John Wiley & Sons.
78. Bludov, Y.V., Ferreira, A., Peres, N., and Vasilevskiy, M. *A primer on surface plasmon-polaritons in graphene.* International Journal of Modern Physics B, 2013. **27**(10).
79. Hunsperger, R.G. *Integrated Optics: Theory And Technology*. 2002: Springer.
80. Snyder, A.W. and Lowe, J. *Optical Waveguide Theory*. Vol. 190. 1983: Springer.
81. Blake, L.V. *Transmission Lines And Waveguides*. 1969.
82. Pozar, D.M. *Microwave Engineering*. 2009: John Wiley & Sons, New York, U.S.A.
83. Hertel, P. *Continuum Physics*. 2012: Springer. Germany
84. Chen, C.-L. *Foundations For Guided-Wave Optics*. 2006: John Wiley & Sons.
85. Hanson, G.W. *Quasi-Transverse Electromagnetic Modes Supported By A Graphene Parallel-Plate Waveguide.* Journal of Applied Physics, 2008. **104**(8): p. 084314.
86. Niu, W., Huang, M., Xiao, Z., Zheng, L., and Yang, J. *Sensitivity Enhancement In TE Mode Nonlinear Planar Optical Waveguide Sensor With Metamaterial Layer.* Optik-International Journal for Light and Electron Optics, 2012. **123**(6): p. 547-552.
87. Stauber, T., N. Peres, and A. Geim. *Optical Conductivity Of Graphene In The Visible Region Of The Spectrum.* Physical Review B, 2008. **78**(8): p. 085432.
88. Falkovsky, L. and A. Varlamov. *Space-Time Dispersion Of Graphene Conductivity.* The European Physical Journal B, 2007. **56**(4): p. 281-284.
89. Mikhailov, S. and K. Ziegler. *Nonlinear Electromagnetic Response Of Graphene: Frequency Multiplication And The Self-Consistent-Field Effects.* Journal of Physics: Condensed Matter, 2008. **20**(38): p. 384204.